Characterising the heterogeneous nature of tufa mounds by integrating petrographic, petrophysical, acoustic and electromagnetic measurements

Characterising the heterogeneous nature of tufa mounds by integrating petrographic, petrophysical, acoustic and electromagnetic measurements

Schröder, S.[a*]; Corella, J.P.[b]; Pellicer, X.M.[c#]; Rook, P.[a]; Kara, A.[a]; Comas, X.[d]

a: Department of Earth and Environmental Sciences, University of Manchester, Manchester M13 9PL, UK, E-mail: stefan.schroeder@manchester.ac.uk

b: CIEMAT - Environmental Department (DMA), Avenida Complutense 40, E-28040 Madrid, Spain

c: Geological Survey Ireland, Beggars Bush, Haddington Road, Dublin 4, Ireland

d: Department of Geosciences, Florida Atlantic University, Davie, USA

*: Corresponding author

#: Now at Orígens UNESCO Global Geopark, Tremp, Spain

Abstract

Determination of the physical properties of subsurface geological bodies is essential for georesource management and geotechnical applications. In the absence of direct measurements, this usually passes via geophysical methods such as seismic and ground-penetrating radar. These require conversion to physical properties, and measurements at different scales to test for consistency. This approach is non-trivial in geobodies with heterogeneous patterns of properties. Tufa mounds - in-situ terrestrial carbonate buildups precipitating from geothermal waters – are characterised by high contrasts in facies and petrophysical properties from microscale to macroscale, and are therefore ideally suited to test the ability of non-invasive geophysical methods to estimate such contrasts, and to develop petrophysical models based on geophysical properties. Here, a laboratory-based study of a Pleistocene tufa mound in Spain is presented that combines (1) petrography, (2) digital 2D pore network analysis, (3) gas porosity and permeability measurements,

(4) acoustic velocity measurements, and (5) electromagnetic wave velocity and porosity determination from ground-penetrating radar, to develop empirical petrophysical models. These results show the consistency of petrophysical properties determined with different methods across various observational scales. Electromagnetically-derived porosity positively correlates with gas porosity. Petrophysical properties depend on measurable rock fabric parameters and the degree of cementation, which provide predictive tools for subsurface geobodies. Strongly cemented peloidal-thrombolitic fabrics with intergranular and intercrystalline pores, and a dominance of small complex pores best transmit acoustic waves. Weak cementation and a significant fraction of large simple pores (framework, vegetation moulds) increase porosity and permeability of shrubby fabrics, while causing lower acoustic velocity. This study demonstrates that ground-penetrating radar models can be used in combination with direct measurements of physical subsurface properties to capture highly contrasting physical properties associated with different sedimentary facies that would not be achievable with other methods, thus improving the understanding of formational processes.

Key words: acoustic properties, electromagnetic properties, ground-penetrating radar, porosity, tufa mounds

1 Introduction

Geophysical methods have been routinely applied for decades to infer petrophysical properties of the subsurface. Early studies include the characterisation of geological reservoirs using electrical methods (Archie, 1942; Schön, 2011; Waxman & Smits, 1968), or empirical models to describe the permittivity behaviour of natural liquids, solids, or mixtures of both (Cole & Cole, 1941). Other more recent studies include efforts to link seismic interpretation to petrophysical properties of the subsurface via data inversion (Bosch, 2004), amplitude versus offset (Yardley et al., 1991), or attribute analysis (Possato et al., 1984). Advantages of these methods over other approaches such as coring include their minimally invasive nature, the wide range of sampling volumes, or the potential for high-resolution measurements (Koesoemadinata & McMechan, 2003). However, there is a need for calibration in order to convert geophysical signatures into physical properties. For example, correct interpretation of seismic data depends on properly correlating the seismic response to the rock lithological and petrophysical properties, such as porosity and density, for which more than one solution may be possible (Kearey et al., 2002). This is non-trivial in carbonate rocks where impedance variations depend less on compositional changes, but – since all carbonate minerals have similar elastic properties – on complex and interrelated variations in fabric, porosity, pore type, pore geometry and diagenesis (Anselmetti & Eberli, 1993; Weger et al., 2009). An increasing body of literature has examined the controls on carbonate seismic response (Anselmetti & Eberli, 1993; Eberli et al., 2003; Weger et al., 2009), including the use of micro computed tomography (microCT), nuclear magnetic resonance (NMR) and pore network analysis to quantify controlling factors (Archilha et al., 2016; Bailly et al., 2022; Reijmer et al., 2022; Ronchi & Cruciani, 2015; Soete et al., 2015; Vasquez et al., 2019; Weger et al., 2009). Analogue data sets from buried carbonate systems as well as outcrops provide 2D and 3D constraints on geobodies and their seismic response.

Similar to seismic reflection methods, ground-penetrating radar (GPR) has been used extensively to link electromagnetic (EM) parameters, such as bulk dielectric permittivity, to subsurface petrophysical properties (Baker et al., 2001). This occurs via calibration of different mixing models that express the bulk dielectric permittivity in a system of solid, liquid and gas phases (Birchak et al., 1974; Huisman et al., 2003). Despite a large body of both field and laboratory-based studies using GPR over the last four decades to estimate petrophysical properties in carbonates (Conti et al., 2019; Cunningham, 2004; Harbi & McMechan, 2011; Mount & Comas, 2014; Mount et al., 2014), few studies have combined methodologies to specifically test the correspondence between physical parameters estimated with different methods (i.e. seismic versus GPR; Al-Shuhail & Adetunji, 2016; Ghose & Slob, 2006; Koesoemadinata & McMechan, 2003). The combination of these complementary techniques can more reliably determine parameters such as porosity and water saturation, and provide input to numerical modelling, particularly in geobodies characterised by markedly heterogenous architecture of facies and physical properties that may offer information on formational processes. A good example of such geobodies are continental carbonate tufas where a complex interplay of physico-chemical and biological processes, and secondary diagenetic overprint result in a heterogeneous network of primary and secondary pore types at a range of scales (Armenteros, 2010; De Boever et al., 2017; Della Porta, 2015). Semi-lithified tufas are ideally suited to reconstruct 3D geobodies using electromagnetic methods (Linares et al., 2010; Pedley et al., 2000; Pellicer et al., 2014).

This study investigates the Isona Tufa Mound Complex (ITMC, North-East Iberian Peninsula), which displays a wide range of subaerial tufa facies. The study expands on previous geophysical surveys in the area (Pellicer et al., 2014), by applying a combination of petrophysical, acoustic and electromagnetic methods constrained with direct petrographic and mineralogical measurements at the laboratory scale. The approach is used to infer changes in the physical properties (i.e. porosity, permeability, or dielectric permittivity) for different distinctive facies of the ITMC. The results show the complementary nature of these measurements, allowing further definition of the spatial variability of physical properties in these unique environments.

2 Geological setting and study site

Tufas of the ITMC are located in the Tremp Basin, an E-W trending structural piggy-back basin deformed and carried southwards by the Montsec thrust during the Pyrenean orogeny (Figure 1A; Vergés et al., 2002). Local topography reflects the underlying geology that developed during thrusting: the basin is bound to the north by the Boixols thrust and San Corneli hanging wall anticline, and to the south by the Montsec range, which developed above the Montsec thrust (Figure 1A; Puigdefabregas et al., 1992; Vergés et al., 2002). Upper Cretaceous – Eocene syn-orogenic sediments fill the Tremp Basin (Vergés et al., 2002). Marine conditions lasted until the latest Upper Cretaceous, when shallow-water carbonates, deep-water marls and the deltaic sandstones of the Aren Formation were deposited (Nagtegaal et al., 1983). Progressive basin fill established continental conditions in the uppermost Maastrichtian; these are recorded by red claystones, coarse siliciclastics and carbonates of the Tremp Group (Pujalte & Schmitz, 2005; Rosell et al., 2001).

The ITMC is located in a continuation of the Isona anticline, a secondary fold structure plunging west (Figure 1A). The mound complex developed over an artesian spring system (Linares et al., 2010). The groundwater recharge area includes Aren Formation sandstones and the updip area of the Isona anticline (Linares et al., 2010) outcropping north and east of the ITMC. In addition, the Upper Cretaceous karstified limestone bedrock along the Montsec range to the south is hydraulically connected with the Aren sandstone aquifer (Figure 1A). This aquifer carries HCO_3^--rich water into the Tremp Basin, where the overlying Tremp Formation acts as an aquitard (Linares et al., 2010; Rosell et al., 1994). Fracturing and erosional thinning of the aquitard, as well as denudation of topography to below the piezometric surface, allows groundwater discharge, and the establishment of an artesian spring system along the buried crest of the Isona anticline (Linares et al., 2010).

The ITMC forms a mesa caprock about 9 km^2 in area, and contains several discharge outlets with tufa deposits aligned along E-W and N-S trending faults (Figure 1B). Deposits represent subaerial carbonate precipitation from an artesian karstic groundwater system with water temperatures of 14.8 to 18.8°C (Linares et al., 2010). Tufa deposits are mapped as three distinct morpho-stratigraphic units (Figure 1B; Pellicer et al., 2014):

(1) Three inactive outlets located on the 'Mont de Conques' mesa (Figure 1B) comprise 47 m thick tufa deposits with ages older than 350 ka (Linares et al., 2010).

(2) A series of fossil mounds formed between >350 and 214 ±11 ka (Linares et al., 2010), occur at lower elevation west and north of the oldest mound.

(3) The youngest mounds with tufa deposits reaching up to 10 m thickness and ages ranging from 6 to 103 ka (Linares et al., 2010) are located in the northern area of the ITMC. These are associated with active groundwater outlets forming circular lakes (Basturs lakes).

3 Materials and methods

A combination of petrographic, petrophysical, acoustic and electromagnetic measurements were carried out in the laboratory to characterise the physical properties of selected carbonate samples.

3.1 Sampling and petrography

Samples for this study cover the whole age range of the ITMC (Figure 1B), and represent lithified carbonates from five facies (Table 1; details in Section 4.1). Blocks were plugged both parallel and vertical to depositional features such as lamination, and plugs trimmed for thin section preparation. Petrographic analysis of 11 thin sections was conducted under transmitted light to characterise depositional fabrics, cementation and pore geometries. Cementation was estimated on thin sections. Plugs were carefully trimmed for a cylindrical shape (diameter 2.5 cm, length 4.0-8.8 cm) without fractures or chipped surfaces, which would disturb petrophysical measurements. Anisotropy in the plugs could lead to poor wave propagation through the plugs causing poor wave picks and unrepresentative results (Singh, 2007). Plugs were used for determination of porosity, permeability and acoustic properties.

A second set of limestone blocks (approximate dimensions 40x20x20 cm) were trimmed by saw in the field. These were used both for laboratory-based electromagnetic measurements, as well as determination of porosity and permeability on plugs cut from the blocks.

3.2 Digital image analysis (DIA) of pore space

Thirteen representative thin section photographs from all five facies were analysed for 2D pore shape parameters using ImageJ© software (Table 2). The software allowed manual segmentation of high-resolution photographs into pore space and rock matrix. The resulting binary images were edited with the Despeckle and Fill Holes filters in ImageJ© to remove individual pixels and holes. Each image was manually checked to remove pixels along image edges, as well as erroneous data such as air bubbles that falsified segmented pore shapes, and non-porosity that was segmented together with porosity. At the selected image resolution, individual pixels had a size of about 3x3 μm, and so pore shape parameters were calculated on pixels with an area ≥10 μm^2 to further filter out individual pixels. The following 2D shape parameters were measured, following standard practice in earlier studies (Weger et al., 2009):

- Area (in mm^2) of segmented pores, median pore area (in mm^2) and total thin section porosity (as a fraction of photograph area). As measured pore areas span a large range from 11 μm^2 to 2.5 mm^2, they were grouped into 20 logarithmic classes analogous to the phi grain size scale.
- Dominant pore size (DomSize) calculated as the upper boundary of pore areas making up at least 50% of thin section porosity. It is given as the radius (in µm) of a sphere with the same area. This parameter indicates the pore size dominating the sample.
- Perimeter measures the length of the outside boundary of a pore (in mm).
- Perimeter over Area (PoA), calculated as the ratio of perimeter and pore area (in mm^{-1}). High values correspond to more complex pore shapes.
- Circularity, calculated as $4\pi \times \frac{Area}{Perimeter^2}$ (Eq 1)

  with a value of 1 indicating a perfect circle, and increasingly elongate shapes as the value approaches 0.
- Aspect ratio (AR) is the ratio of major and minor axes of an ellipse fitted to the pore.

3.3 Porosity and permeability measurement

Petrophysical data were acquired on 18 plugs (Table 3). Porosity was calculated using measurements of bulk volume (V_b) and grain volume (V_g). Plugs were dried in an oven to remove bound water as this could affect the bulk volume. Each plug was heated to 60°C and weighed every 10 mins until the drop-off in mass became negligible. After cooling, the length and diameter of each plug was measured using a caliper. Each plug was measured six times in different places to calculate an average value of cylinder volume V_b.

Equilibrium pressure was measured using a ResLab™ DHP-100 digital helium porosimeter. After calibration using samples of known volumes, equilibrium pressure was measured by letting helium gas expand into the sample chamber of known volume. These measurements were repeated three times per sample. Samples were left for 30 mins between each run to reduce the chance of residual gas affecting subsequent results. These measurements were used to calculate grain volume V_g for each sample using Boyle's law. Once grain volume was calculated, porosity was determined by:

$$\phi = \frac{V_b - V_g}{V_b} \quad \text{(Eq 2)}$$

Porosity values were averaged using the three measurements of V_g.

A ResLab™ DGP-200 digital gas permeameter calibrated for nitrogen gas was used to measure permeability using a steady state method. After completely confining each plug in a rubber jacket-lined core holder under *ca* 1.8 MPa confining pressure, nitrogen was allowed to flow through each plug. This flow was adjusted until the differential pressure in the jacket equilibrated. Three runs were performed per sample and an average value calculated to increase result accuracy. Each sample was left for 30 mins to allow gas to filter out between each run. The differential pressure could then be used to calculate permeability using Darcy's law. Viscosity is temperature dependent and was calculated based on the temperature displayed by the permeameter.

<u>3.4 Laboratory-based acoustic velocity analysis</u>

Acoustic velocities of p-waves (Vp) and s-waves (Vs) were determined on 12 plugs with benchtop equipment at ambient conditions (Table 3). Due to the fragile nature of samples, no measurements under confining pressure were carried out. Measurements determined the travel time of an ultrasonic pulse through the core plug. The signal was generated by a Tektronix AFG 2021 signal generator and fed through a Falco System amplifier to produce a wave of 18 ns and 100 v. The sample was held in a vice between two transducers smeared with ultrasound gel to aid wave propagation. The vice generates a small (<0.5 MPa) pressure on the samples. The wave was picked up by a LeCroy Wave-ace 1002 60 MHz oscilloscope. Dead time of the transducers was also calculated and subtracted from the measured values. A different set of transducers was used for both P and S waves. The velocity was then calculated based on the distance-time ratio. Acoustic velocities served to calculate Poisson's ratio according to equation:

$$\upsilon = \frac{1}{2} \times \frac{(V_p{}^2 - 2 \times V_S{}^2)}{(V_p{}^2 - V_S{}^2)} \qquad \text{(Eq 3)}$$

The acoustic impedance Z is given by the equation:

$$Z = \rho \times V_p \qquad \text{(Eq 4)}$$

where ρ is density and Vp the p-wave velocity.

Time average equations relate porosity and acoustic velocity based on theoretical and empirical considerations. The two equations applied here are the Wyllie Time Average (WTA) and Raymer-Hunt-Gardner (RHG) equations (Raymer et al., 1980; Wyllie et al., 1958):

$$\frac{1}{V_P} = \frac{\phi}{V_{P\,fl}} + \frac{1-\phi}{V_{P\,min}} \qquad \text{(WTA; Eq 5)}$$

$$V_P = (1-\phi)^2 \times V_{P\,min} + \phi \times V_{P\,fl} \qquad \text{(RHG; Eq 6)}$$

where Vp_{min} and Vp_{fl} are acoustic velocity in the mineral matrix, and pore fluid, respectively (m s^{-1}).

3.5 Laboratory-based electromagnetic velocity analysis

A Mala ProEx GPR system paired with two 1,200 MHz GPR antennas were used in the laboratory to estimate EM wave velocity along seven sample blocks in transmission mode (Table 4). In this mode, only EM waves traveling one-way from the transmitter to receiver are used (instead of reflections). Measurements were collected for a total of seven samples and under two different conditions, 1) fully dry; and 2) fully saturated. In each case, an EM wave velocity is calculated through:

$$\upsilon = \frac{c}{\sqrt{\varepsilon_{r(b)}}} \qquad \text{(Eq 7)}$$

where v is velocity (m ns^{-1}), c is a constant (0.3 m ns^{-1}) and $\varepsilon_{r(b)}$ is the bulk dielectric permittivity of the material. The distance that the EM wave will travel through the material allows calculation of v and thus the calculation of $\varepsilon_{r(b)}$. This permittivity is then used to apply a petrophysical model, the Complex Refractive Index Model (CRIM). The CRIM is a three-phase dielectric mixing model that can be used to express the bulk dielectric permittivity of a solid, liquid and gas in a system (Huisman et al., 2003, Robinson et al., 2003). The CRIM expresses the bulk relative dielectric permittivity ($\varepsilon_{r(b)}$) as:

$$\varepsilon_{r(b)}{}^{\alpha} = \phi S_w \varepsilon_{r(w)}{}^{\alpha} + (1-\phi)\varepsilon_{r(s)}{}^{\alpha} + \phi(1-S_w)\varepsilon_{r(a)}{}^{\alpha} \qquad \text{(Eq 8)}$$

where $\varepsilon_{r(s)}$ is the relative dielectric permittivity of limestone (i.e. solid phase with specific values), $\varepsilon_{r(a)}$ and $\varepsilon_{r(w)}$ are the relative dielectric permittivity of air (1) and water (79.5) based on water temperature in the sample measured at 22°C (Buchner et al., 1999), ϕ is the porosity, and S_w is the water saturation with values between 0 and 1, with 0 and 1 representing fully dry and saturated conditions, respectively. The factor α accounts for the orientation of the electrical field with respect to the geometry of the limestone, with values between -1 and 1, with 0.5 being used here as explained below. By obtaining both dry and wet EM wave velocity, a system of two equations can be generated from equation 4. These equations are characterised by a unique $\varepsilon_{r(b)}$, and a S_w equal to 1 or zero for completely saturated and dry conditions respectively, allowing for the isolation of both n and $\varepsilon_{r(s)}$. This approach follows the laboratory setup described in Mount and Comas (2014).

3.6 X-ray diffraction

Mineralogy of eight samples from all facies was determined by X-ray diffraction. Analyses were conducted using a Bruker D8 Advance Diffractometer (Cu Kα X-Ray source) at the Williamson Research Centre (University of Manchester). Samples were scanned from 5 to 70° 2θ, using a step size of 0.02° and a counting time of 0.2 seconds per step.

4 Results

4.1 Tufa facies, petrography and mineralogy

4.1.1 Facies

Inactive and modern outlets and deposits can be subdivided into five facies representing distinct tufa sub-environments (Figure 2; Table 1). The central part of most inactive mounds and the modern lakes forms sub-circular pool depressions 30 to 140 m in diameter (Figure 2; Pellicer et al., 2014). Apart from the modern lakes, these depressions are filled by basal unlithified palustrine lime muds with oncoids, coated grains and stromatolites (Pellicer et al., 2014), overlain by detrital sediments reworked from the rim of the enclosed depression following lake desiccation (Pellicer et al., 2016). Locally in the 'La Cassola' mound, vents that acted as fluid conduits, are preserved within the pool (Pellicer et al., 2014). Vents form largely circular geobodies, are several metres in diameter, and rise about 1 m above the ground. The pool is separated from the outward-facing slopes by a rim composed of a limestone ridge that rises 0.5 to 1 m above the pool ground (Figure 2; Pellicer et al., 2014). Slopes have angles of 5 to 7° in each direction (Figure 2) and are characterised by a stepped morphology of terracettes, microgours and channels (Table 1; Pellicer et al., 2014). Beds are subparallel to the morphological surface. North of the Basturs lakes, cascades drape the topography along the Abella River left bank and near active spring outlets (Pellicer et al., 2014). These consist of parallel beds with dips of up to 40°. Cascades generally are the youngest deposits from *ca* 6 ka to sub-recent (Linares et al., 2010).

4.1.2 Petrography

All samples were crystalline and consisted of >99.5% calcite. A matrix density of 2.71 g/cm^3 was therefore assumed for all further analyses. Petrographically, the samples represent five lithotypes (Table 1). The peloidal lithotype is dominated by peloids embedded in microspar and 30 to 40% equigranular sparite (Figure 3A,B). This creates a granular-crystalline fabric with intergranular, intercrystalline, vuggy pores and fractures (Figure 3B). The outline of the intercrystalline pores is largely determined by the crystals surrounding them, and thus tends to be irregular (Figure 3B). Some of the pores have remains of organic matter, likely from plants.

A thrombolitic lithotype contains thrombolite mesoclots made from clumped peloids, sparry shrubs (see below), and shells (ostracods, gastropods) (Figure 3C,D). Mesoclots define a growth framework with framework and mouldic porosity. Cements (20-35%) either line the larger pores as blocky sparite, or completely fill the smaller pores as drusy sparite (Figure 3D).

A framework of sparry shrubs and peloids constitutes the sparry shrub lithotype. Shrubs are locally arranged in beds, and cemented by small sparite crystals (Figure 3E,F). The sparry shrubs consist of sparite crystals forming around hollow or micrite-filled upright and branching tubes (Figure 3G). They are equivalent to the spar-rhomb shrubs described by Guo and Riding (1994, 1998), and the sparry filaments of Gradzinski (2010). Cements make up 5 to 15% of the thin sections, but can increase to 20 to 25% where sparry shrubs are better developed. Pore types include intercrystalline pores between the small sparite crystals (Figure 3F), growth framework and vegetation moulds, possibly after bryophytes (Figure 3H) (Melón & Alonso-Zarza, 2018).

The peloidal shrub lithotype (Figure 4A,B) shares the abundance of peloids with peloidal and thrombolitic fabrics. Peloids can be arranged into peloidal shrubs (Figure 4B), which are analogous to micritic shrubs of Guo and Riding (1994) or micritic dendrites of Della Porta (2015). Pore types include intercrystalline, framework, vuggy and vegetation moulds (Figure 4A,B). Equigranular and acicular cements make up 25 to 35% of the thin sections.

The oncoidal lithotype (Figure 4C,D) consists of millimetre-scale oncoids in a groundmass of partly clotted (peloidal) micrite. The oncoid core is porous microspar and clotted micrite, surrounded by wavy laminae and botryoids (Figure 4D). Porosity is mostly intergranular and intercrystalline. Vegetation moulds and vuggy porosity are associated. Cement is essentially microspar, constituting 15 to 25% of thin sections.

In summary, vent facies are associated with the peloidal lithotype (Table 1). Samples from the older 'La Cassola' rim (sample RM-09) have the thrombolitic lithotype, whereas their younger counterparts at the 'Basturs' rim (sample RM-07) consist of the sparry shrub lithotype (Table 1). The cascade facies is associated with the sparry shrub lithotype, and the pool lithified stromatolites have the oncoidal lithotype (Table 1). A gradation of lithotypes is observed in the slope samples. Slopes from the older 'La Cassola' mound are dominated by the peloidal lithotype (sample SL-10). On the younger 'Basturs' slope, peloidal shrub (sample SL-05) and sparry shrub lithotypes (sample SL-02) dominate. Generally speaking, the sparry shrub lithotype is only lightly cemented (< 15-25 %) and only occurs in the younger 'Basturs' samples. The other lithotypes tend to be more compact and more cemented (< 40 %), and they are the only lithotypes present in the older 'La Cassola' samples.

4.2 Petrophysical and acoustic properties

Petrophysical measurements resulted in gas porosity and permeability from 18.5 to 43.0 %, and 2 to 14,000 mD, respectively (Table 3), showing a statistically significant positive linear correlation between the two variables (R^2=0.5438, R<0.005; Figure 5A). The lowest porosity and permeability values occur in vent and older ('La Cassola' mound) rimstone samples (peloidal and thrombolite lithotypes), whereas the highest values are in the sparry shrub lithotype of the younger ('Basturs') cascade and rim facies (Table 3, Figure 5A). In slope samples, an increase of sparry shrubs at the expense of peloids (sample SL-10 to SL-02) parallels an increase in porosity and, to a lesser extent, in permeability (Figure 5A). No porosity and permeability data were obtained for the pool facies (oncoidal lithotype), as samples were damaged during preparation. Given the high porosity and permeability of cascade samples, it was difficult to maintain laminar flow during analysis, and the values obtained may overestimate actual porosity and permeability.

Acoustic measurements resulted in Vp values from 2,055 m/s to 6,197 m/s, while Vs ranges from 901 m/s to 2,859 m/s (Table 3, Figure 5B). In both cases, a statistically significant inverse linear correlation exists between porosity and acoustic velocity. The highest velocities occur in vent and older rim facies (peloidal and thrombolitic lithotypes) (Vp = 5,670-6,197 m/s; Vs = 2,573-2,859 m/s), whereas the lowest values correspond to cascade samples (sparry shrub lithotype) (Table 3, Figure 5B). Similarly, a strong inverse correlation also exists between gas porosity and acoustic impedance (Figure Supplementary Material 1), with values ranging between 2.3 Ns/m^3 (cascade) and 12.4 Ns/m^3 (rim). In porosity-acoustic velocity space, most data significantly deviate positively from time average curves (Figure 6), so that time average curves will underestimate Vp values for a given porosity. The divergence is strongest for peloidal and thrombolitic lithotypes at the high-Vp end of this study. The Vp/Vs ratios for ITMC samples fall between 1.5 and 2.3 (Table 3). Acoustic velocity and Poisson's ratio covary (Figure 7). Peloidal and thrombolitic lithotypes cluster at high velocities and Poisson's ratios, whereas the sparry lithotype dominates at the lower end. Two low-Vp samples (CS-01 and SL-10) fall outside of the central data trend. If these are excluded, the correlation is good and statistically relevant (R^2=0.788, P<0.005); otherwise it is poor and statistically insignificant (R^2=0.259, P=0.091).

4.3 Pore shape analysis

Although thin section porosity calculated from DIA consistently underestimates gas porosity measurements, there is a positive correlation between both (Figure Supplementary Material 2A), with a correlation coefficient R^2=0.765 and P<0.005 (Table 2). Digital image analysis correctly replicates the low porosity of thrombolitic and peloidal lithotypes, and the high porosity of the sparry shrub lithotype (Figure Supplementary Material 2A). In a diagram of cumulative pore area distributions (Figure 8), high-Vp samples (VT-08 and SL-10; peloidal lithotype) tend to have normal distributions with a 50 percentile in the range 7.3 to 14.5 x 10^5 mm^2. As sample porosity increases and Vp decreases (cascade and high-porosity rim and slope samples CS-01, SL-02 and RM-07, with sparry shrub lithotype), pore-size distributions develop a marked tail of larger pore sizes, and the 50 percentile increases to 12.0 to 44.0 x 10^5 mm^2 (Figure 8). The exception here is sample RM-09 (thrombolitic lithotype), which despite having the lowest measured porosity, has an intermediate 50 percentile (11.0-19.0 x 10^5 mm^2) and a distinct tail of larger pores (Figure 8). This is consistent with the thin section observation of mainly larger framework pores between mesoclots.

The relationship between DomSize and gas or thin section porosity is weak (DomSize of low-porosity samples 9.1-223.7 μm, or 9.1-18.4 μm if sample RM-09 is excluded; DomSize of high-porosity samples 120.9-180.6 μm; R^2=0.146, P<0.005; Figure Supplementary Material 2B). The high DomSize of sample RM-09 (138.6-223.7 μm) reflects the dominance of framework pores between mesoclots. The sample aspect ratios and circularity do not show a relationship amongst themselves or with pore size parameters. On the other hand, there is an inverse relationship between median PoA and median pore size or DomSize (Figure 9, Figure Supplementary Material-3). Samples with lower porosity and higher Vp (samples VT-08, SL-10; peloidal and peloidal shrub lithotypes) cluster at the high PoA end (451.5-527.8 mm^{-1}), whereas samples with higher porosity and lower Vp (CS-01, SL-02 and RM-07, sparry shrub lithotype) preferentially occur at the low PoA end of the spectrum (229.5-382.5 mm^{-1}).

The digital image analysis demonstrates that low-porosity, high-Vp samples tend to have the peloidal lithotype (Figures 5B, 8 and 9), which is dominated by intergranular and intercrystalline pore types. These pores tend to be small and have a more irregular 2D outline due to polygonal crystalline margins (Figure 3B). As porosity increases (and Vp decreases), larger pores become more important in peloidal shrub and sparry shrub lithotypes (Figures 3F, 4B, 5B, 8 and 9). These are mainly mouldic pores after vegetation, as well as framework and vuggy pores (Figure 3F,H). The outline of these pores is simpler and smoother, reflected in their lower median PoA. Samples RM-09 and SL-05 form exceptions, with intermediate to very high PoA values (314.6-557.1 mm^{-1}) despite having high and intermediate velocities, respectively. The rock fabric of sample SL-05, although a peloidal shrub lithotype, has a high proportion of smaller intercrystalline pores, and so is similar to the peloidal lithotype. This is combined with larger framework pores that contribute to elevated porosity and lower Vp in this sample. Although framework pores dominate in sample RM-09 and create the tail in the pore area distribution (Figure 8), pores are lined or completely filled by well-developed cements, which contribute to lower porosity and higher Vp.

4.4 Electromagnetic properties

Electromagnetic measurements gave values between 0.185 m/ns and 0.101 m/ns for dry conditions, and from 0.059 m/ns to 0.999 m/ns for fully saturated conditions (Table 4; Figure 10). Solving equation (8) provided GPR estimated solid dielectric permittivity (ε) values between 3.4 and 5.7, and porosity values ranging from 10 to 46% (Table 4), with a linear inverse correlation between the two (Figure 11). Slope and cascade samples CS-01 and SL-05 were too brittle during analysis, and therefore no measurements under saturated conditions were possible.

5 Discussion

5.1 Controls on petrophysical and acoustic properties

The petrophysical and acoustic data (porosity, permeability and velocity) show clear relationships amongst each other. Whereas a positive correlation exists between porosity and permeability (Figure 5A), data span a large range, and permeability varies for a given porosity. This reflects the inherent heterogeneity of carbonate pore systems, in particular in continental carbonates (De Boever et al., 2017; Soete et al., 2015). The inverse relationship of porosity and Vp (Figure 6) is well known for carbonates (Anselmetti & Eberli, 1993). Acoustic velocity is a function of bulk density (Kearey et al., 2002). Carbonate systems generally exclude large variations in matrix density, and carbonate minerals have very similar elastic properties (Anselmetti & Eberli, 1993; Verwer et al., 2008). Consequently, bulk density in almost pure carbonate systems such as the ITMC will depend strongly on porosity, hence the observed inverse relationship (Anselmetti & Eberli, 1993; Verwer et al., 2008).

Porosity and velocity data from this study are consistent with previously published data from marine and continental carbonates, and specifically continental tufas and travertines (Figure 6;

Bailly et al., 2022; Eberli et al., 2012; Regnet et al., 2019; Reijmer et al., 2022; Soete et al., 2015; Vasquez et al., 2019; Weger et al., 2009). Datasets were variably obtained at ambient and confined pressures; the only tufa and travertine dataset shown that was measured under confined pressure is from Soete et al. (2015). It may be shifted to higher velocities due to faster wave transmission at confining pressure. The ITMC dataset has somewhat higher porosity and/or velocity values relative to the other tufa and travertine datasets. Despite the large natural heterogeneities in these lithologies, tufa and travertine datasets remain, however, broadly consistent.

All datasets diverge to higher Vp values from time average curves, and this divergence is most prominent in continental tufas and travertines (Figure 6; Bailly et al., 2022; Soete et al., 2015). In the ITMC, mineralogy is predominantly calcite, and thus the large velocity and impedance variation cannot relate to mineralogical variations, such as clay minerals, which are commonly invoked for marine and lacustrine carbonates (Bailly et al., 2022; Regnet et al., 2019; Reijmer et al., 2022; Weger et al., 2009). Instead, velocity variations are most likely a function of changes in rock fabric, pore type and pore geometry (Anselmetti & Eberli, 1993; Weger et al., 2009). The positive correlation between Vp and Poisson's ratio in the ITMC (Figure 7) reflects a crystalline rock fabric, which has different acoustic behaviour than purely granular fabrics (Kenter et al., 2007). The development of an indurated framework at deposition is further supported by the observed Vp/Vs ratios for ITMC samples (1.5-2.3, Table 2) that largely fall within the range considered normal for indurated carbonates (1.8-2.2; Anselmetti & Eberli, 1993). The crystalline rock framework of travertines and tufas consists of framestones and cementstones with considerable compressive and shear strength (Soete et al., 2015). They often contain mechanically stiff mouldic and vuggy pores (Xu & Payne, 2009) that explain the positive Vp divergence. The cascade sample has the highest Vp/Vs (2.3) and highest Poisson's ratio (0.38). This anomalous behaviour can relate to Vs values dropping off relative to Vp values in highly porous fabrics

(Anselmetti & Eberli, 1993; Pickett, 1963), during closure of microcracks (Reijmer et al., 2022), or can be an analytical artifact.

In the ITMC, the relationship between rock fabric parameters and acoustic-petrophysical properties is approximated by variations between two fabric end members. Samples with high velocity and low porosity are dominated by peloidal and thrombolitic lithotypes with intergranular and intercrystalline pores (Figure 5B). The original granular fabric is strongly overprinted by microspar and equigranular cement (Figure 3B), the latter forming extensive bridges between grains (Figure 3B,D), together creating a very crystalline fabric. Interlocking crystals and the high degree of cementation create numerous contact points and longer contact lengths, which enhance acoustic wave propagation (Bailly et al., 2022; Eberli et al., 2003; Kenter et al., 2007: Storvoll & Bjørlykke, 2004). The more irregular pore shapes reduce permeability, but equally contribute to wave transmission (Archilha et al., 2016). Therefore, at one end of the spectrum in the ITMC, irregular and small pores, higher degree of cementation and interlocking crystalline fabric are likely key factors for the observed acoustic and petrophysical properties.

At the other end of the spectrum, the sparry shrub lithotype contains a tail of large macropores with relatively smoother outlines (Figures 8 and 9). To a large degree these are framework pores and vegetation moulds that were only lightly coated by cement crystals (Figure 3F,H). These macropores are visually very well connected, and the relatively low degree of cementation largely preserves open pore throats, favouring high permeabilities (Figure 5A). Intercrystalline porosity occurs between the crystals, adding to the high porosity of this fabric (Figure 3F). This very open crystalline framework with a combination of larger and smaller pores provides a lower number and area of framework contacts, but will equally promote scattering of acoustic waves (Soete et al., 2015). Both factors will reduce wave velocities. Finally, the acoustic velocities of some of these highly porous (>35%) samples are lower than predicted by the Wyllie equation (Figure 6;

Anselmetti & Eberli, 1993; Pickett, 1963). The elastic rigidity of the hollow framework characteristic for the sparry shrub lithotype is low compared to marine frameworks such as corals, causing slower sonic velocities relative to predictions (Soete et al., 2015). Presence of micropores and microcracks (both original as well as artefacts from preparation of the fragile sample material) can also reduce sonic velocities (Bailly et al., 2022; García del Cura et al., 2012; Reijmer et al., 2022; Xu & Payne, 2009).

Between these two endmembers, the peloidal shrub lithotype combines peloids, peloidal shrubs and sparry shrubs in a largely crystalline fabric. Pore types include intercrystalline, vegetation moulds, and elongate framework pores. As the degree of cementation is comparable to peloidal and thrombolitic lithotypes, a key factor for reducing Vp in the peloidal shrub lithotype is the development of more open rock frameworks via mouldic and framework pores that are associated with sparry shrubs. This is clearly visible in the increase in porosity and the decrease in Vp that accompany the increase of sparry shrubs at the expense of peloids in the slope facies (sample SL-10 to SL-02; Figure 5A). Presence of vegetation moulds with a more peloidal-micritic framework tends to stiffen the rock (Bailly et al., 2022, Soete et al., 2015) and cause positive deviation from time average curves.

Acoustic and petrophysical properties in the ITMC are thus a function of development of a crystalline fabric, presence of framework and mouldic pores versus intergranular and intercrystalline pores, and the degree of cementation. As all older ('La Cassola') samples are fairly strongly cemented, and the sparry shrub lithotype has only been observed in the younger ('Basturs') samples, the age of the deposit is a secondary control.

5.2 Controls on electromagnetic (EM) properties

5.2.1 Relationship between porosity and dielectric permittivity

Laboratory-based EM wave velocity estimates under fully dry and saturated conditions are consistent with EM wave velocities estimated in the field for each ITMC morphological element by Pellicer et al. (2014) (Figure 10). At low porosity, the bulk dielectric permittivity is buffered by the dielectric permittivity of the rock matrix, leading to only small variations between saturated and dry conditions (Figure 10; Mount & Comas, 2014). With increasing porosity, the relative contributions of the contrasting dielectric permittivities of water (79.5) versus air (1) will increase (Eq 8), causing a decrease or increase of bulk permittivity, respectively (Figure 10; Neal, 2004; Topp et al., 1980).

Porosity and solid dielectric permittivity estimated from EM measurements show an inverse relationship, however given the limitation in datasets, the correlation coefficient is low ($R^2 = 0.5$; Figure 11) and not statistically significant ($P > 0.05$). As both were unknowns in solving equation (5), coupled variability is to be expected (Mount & Comas, 2014). The determined permittivity data are within the range for carbonate rocks (4-8; Davis & Annan, 1989).

5.2.2 Comparison between measured gas porosity and estimated porosity

The advantage of the approach presented here is that porosity estimates from different analytical methods can be compared. This allows porosity calculation where only individual methods are available. For example, where Vp is available (e.g. from wireline logs), it can be used to estimate porosity via the RHG equation (Eq 6). In the current study, comparing porosity calculated in this way against measured gas porosity, results in a good and statistically significant correlation ($R^2 = 0.823$ and $P < 0.05$; Figure 12). This calculation strongly underestimates measured gas porosity (by a factor of ≤4) at low porosity, but produces similar values at high porosity (Figure 12). As discussed above, due to the dominance of stiff rock frameworks and stiff pores in continental carbonates, the RHG equation would predict lower Vp for a given porosity (Figure 6), so this divergence is to be expected. At highest porosity, lower stiffness of hollow rock frameworks and the effects of microcracks reduce Vp, so the RHG equation better predicts Vp values (Figure 6).

However, given that time average curves do not account for fabric and pore network variation, in particular in crystalline carbonates (Kenter et al., 2007), it may be more appropriate deriving porosity directly from measured velocities on travertine and tufa samples (regression line in Figure 6). For these samples, including those of the ITMC, velocity relates to porosity as:

$$V_P = -6537.3 \times \phi + 6017.1 \qquad \text{(Eq 9)}$$

This results in a good and statistically significant correlation ($R^2 = 0.825$ and $P < 0.05$; Figure 12), which produces similar values as time average curves at low porosities, but diverges to overestimation at high porosities (cf. Soete et al., 2015).

Measured gas porosity and EM porosity determined from the CRIM model show a good linear correlation that is statistically significant ($R^2 = 0.812$ and $P < 0.05$; Figure 12). Porosities relate as:

$$\phi_{EM} = 1.030 \times \phi_{gas} - 0.096 \qquad \text{(Eq 10)}$$

With the exception of one sample, gas porosities are higher (up to a factor of 2.3) than corresponding EM porosities (Figure 12). This shift may relate to incomplete saturation achieved during the EM measurements. If certain pore spaces were not fully saturated, remaining air (permittivity = 1) would cause a higher EM wave velocity, and consequently a lower permittivity and a lower porosity estimate (Mount & Comas, 2014). The helium gas used in petrophysical analysis on the other hand would have been able to enter micropores, and thus gives a more realistic porosity value.

Nevertheless, the comparable trends of gas and EM porosity suggests that the two methods can be combined for estimates of physical properties of subsurface materials. The observed differences may reflect the different behaviour of electromagnetic waves and helium gas during measurements, the scale of observation volume, and rock heterogeneities captured within this volume (cf. Conti et al., 2019; Mount & Comas, 2014; Mount et al., 2014). The latter point is particularly true for continental carbonates. The dependency of porosity measurements on the reference volume being investigated has been recognised in reservoir petrophysics (Bailly et al., 2022; Fitch et al., 2015; Frykman & Deutsch, 2002) and GPR studies (Mount & Comas, 2014; Mount et al., 2014). Combination of analytical techniques at several scales of observation is therefore important for coherent characterisation of subsurface properties. Mount and Comas (2014) have demonstrated consistency in porosity determination between outcrop GPR (metre-scale) and laboratory-based GPR (decimetre-scale) measurements. The present study shows a consistency between laboratory-based GPR and plug petrophysics (millimetre/centimetre-scale).

5.3 Implications for formational processes

The consistency between different methods at predicting physical properties can be related to formational processes in tufa mounds. Methods were consistent at identifying: 1) lowest porosity and permeability, highest velocity, and well-cemented crystalline rock frameworks correspond to older vent and rim facies; 2) highest porosity and permeability, lowest velocity, and less cemented rock frameworks correspond to cascade facies; and 3) intermediate values correspond to slope facies. Previous studies describing evolutionary models for the ITMC tufa mounds (i.e. Linares et al., 2010; Pellicer et al., 2014) used geophysical methods like GPR or electrical resistivity imaging (ERI) to image subsurface contrasts in physical properties (like dielectric permittivity or electrical resistivity), which were then used to interpret a concentric increase in porosity from the centre of the mound (where mound conduits were infilled by chemical precipitates as supersaturated groundwater emerged) to the edges (where cascade and slope facies accumulated below the rimstones). For example, electrical resistivity decreases from the vents towards the outer zones (Linares et al., 2010). In a similar manner, Pellicer et al. (2014) used 2D GPR profiles to define the interfaces between stratigraphic facies based on differences in EM wave amplitude and reflector signature (or radar facies). Given the limitations imposed in this study by the spatial distribution of samples, the limited number of analyses due to the fragile nature of samples, and the inherent geological heterogeneities of tufa carbonates, inferring similar 2D models and capturing the full petrophysical variations of the studied tufas is not possible. Despite these limitations however, correlations between various analytical approaches are fairly strong. This study confirms the increase in porosity from vent and rimstone facies to slope and cascade facies, and is able to tie acoustic, petrophysical and electromagnetic properties to measurable rock fabric parameters. At least the two endmember facies (1 and 2 above) can be differentiated even in the absence of petrographic data. Additional research on this and other tufa complexes, using more samples, will be needed to reinforce these conclusions.

The approach followed in this study thus allows mapping properties from wells or samples, such as porosity or saturation, onto 3D subsurface geometries (Chan & Knight, 1999; Knight, 2001: Neal et al., 2008), which is particularly useful in situations where no direct measurements of subsurface properties are possible. This ability is critical in many groundwater, geotechnical, environmental and reservoir applications (Ghose & Slob, 2006; Greaves et al., 1996; Knight, 2001), and with inclusion of a GPR system in the Mars Perseverance mission, can also constrain hydrogeological conditions on other planets (Pellicer et al., 2014; Rossi et al., 2008).

6 Conclusions

(1) A combined petrophysical (gas porosity, permeability, acoustic velocity, GPR-derived electromagnetic porosity) and petrographic (rock fabrics, pore shape parameters) study was carried out on a Pleistocene tufa carbonate mound. Rocks form a stiff crystalline framework consistent with other examples of continental carbonates. Petrographically, they vary between two endmembers: (1) a peloidal-thrombolitic rock framework with small and geometrically more complex intercrystalline-intergranular pores, and (2) a network of upright sparry shrubs with large and geometrically simpler framework, vegetation mouldic and vuggy pores.

(2) Rock fabric and degree of cementation are the dominant controls on petrophysical and acoustic properties, which accordingly vary between two endmembers. The strongly cemented micritic peloidal and thrombolitic frameworks are more strongly cemented and have low porosity and permeability. The polygonal crystalline framework and cement bridges allow better transmission of acoustic waves. Sparry shrubs have a more open framework with larger pores, limited cementation and reduced crystal-to-crystal contacts, which cause lower acoustic velocities and higher porosity and permeability.

(3) Porosity determined from GPR measurements positively correlates with gas porosity, although it will be lower for a given sample. This is likely an artefact due to inconsistent water and gas saturation of samples during measurements.

(4) In highly heterogeneous materials such as tufa, electromagnetic and petrophysical approaches yield compatible data across a range of observational scales. The study demonstrates that radar models can be compared with direct measurements of physical subsurface properties.

(5) The results of this study support the spatial facies distribution for the tufa mounds derived in previous studies from GPR and resistivity, by confirming an overall concentrically decrease in porosity from the centre to the edges of the mounds. The highly heterogeneous and fragile nature

of tufa samples only allowed collection of a reduced dataset that should be expanded through further studies.

References

Al-Shuhail, A. A. and Adetunji, A. (2016) Joint inversion of ground-penetrating radar and seismic velocities for porosity and water saturation in shallow sediments. *Journal of Environmental and Engineering Geophysics,* 21, 105-119.

Anselmetti, F. S. and Eberli, G. P. (1993) Controls on sonic velocity in carbonates. *Pageoph,* 141, 287-323.

Archie, G. E. (1942) The electrical resistivity log as an aid in determining some reservoir characteristics. *Transactions of the AIME,* 146, 54-62.

Archilha, N. L., Missagia, R. M., Hollis, C., de Ceia, M. A. R., McDonald, S. A., Lima Neto, I. A., Eastwood, D. S. and Lee, P. (2016) Permeability and acoustic velocity controlling factors determined from x-ray tomography images of carbonate rocks. *AAPG Bulletin,* 100, 1289-1309.

Armenteros, I. (2010) Diagenesis of carbonates in continental settings. *In:* Alonso-Zarza, A. M. & Tanner, L. H. (eds.) *Carbonates in continental settings: geochemistry, diagenesis and applications.* Developments in Sedimentology, 62, 61-151. Amsterdam: Elsevier.

Bailly, C., Kernif, T., Hamon, Y., Adelinet, M. and Fortin, J. (2022) Controlling factors of acoustic properties in continental carbonates: Implications for high-resolution seismic imaging. *Marine and Petroleum Geology,* 137, 105518.

Baker, G. S., Steeples, D. W., Schmeissner, C., Pavlovic, M. and Plumb, R. (2001) Near-surface imaging using coincident seismic and GPR data. *Geophysical Research Letters,* 28, 627-630.

Birchak, J. R., Gardner, C. G., Hipp, J. E. and Victor, J. M. (1974) High dielectric constant microwave probes for sensing soil moisture. *Proceedings of the IEEE,* 62, 93-98.

Bosch, M. (2004) The optimization approach to lithological tomography: Combining seismic data and petrophysics for porosity prediction. *Geophysics,* 69, 1272-1282.

Buchner, R., Barthel, J. and Stauber, J. (1999) The dielectric relaxation of water between 0 degrees C and 35 degrees C. *Chemical Physics Letters,* 306, 57-63.

Chan, C. Y. and Knight, R. (1999) Determining water content and saturation from dielectric measurements in layered materials. *Water Resources Research,* 35, 85-93.

Cole, K. S. and Cole, R. H. J. (1941) Dispersion and adsorption in dielectrics. *Chemical Physics,* 9, 341.

Conti, I. M., de Castro, D. L., Bezerra, F. H. and Cazarin, C. L. (2019) Porosity estimation and geometric characterization of fractured and karstified carbonate rocks using GPR data in the Salitre Formation, Brazil. *Pure and Applied Geophysics,* 176, 1673-1689.

Cunningham, K. J. (2004) Application of ground-penetrating radar, digital optical borehole images, and cores for characterization of porosity hydraulic conductivity and paleokarst in the Biscayne aquifer, southeastern Florida, USA. *Journal of Applied Geophysics,* 55, 61-76.

Davis, J. L. and Annan, A. P. (1989) Ground-penetrating radar for high-resolution mapping of soil and rock stratigraphy. *Geophysical Prospecting,* 37, 531-551.

De Boever, E., Brasier, A. T., Foubert, A. and Kele, S. (2017) What do we really know about early diagenesis of non-marine carbonates? *Sedimentary Geology,* 361, 25-51.

Della Porta, G. (2015) Carbonate build-ups in lacustrine, hydrothermal and fluvial settings: comparing depositional geometry, fabric types and geochemical signature. *In:* Bosence, D. W. J., Gibbons, K. A., Le Heron, D. P., Morgan, W. A., Pritchard, T. & Vining, B. A. (eds.) *Microbial carbonates in space and time: Implications for global exploration and production.* Geological Society, London, Special Publication, 418, 17-68.

Eberli, G. P., Baechle, G. T., Anselmetti, F. S. and Incze, M. L. (2003) Factors controlling elastic properties in carbonate sediments and rocks. *The Leading Edge,* July 2013, 654-660.

Eberli, G. P., Verwer, K., della Porta, G. and Weger, R. J. 2012. The role of microbial activity on petrophysical properties (abstract). *AAPG Hedberg Conference Microbial Carbonate Reservoir Characterization.* Houston.

Fitch, P. J. R., Lovell, M. A., Davies, S. J., Pritchard, T. and Harvey, P. K. (2015) An integrated and quantitative approach to petrophysical heterogeneity. *Marine and Petroleum Geology,* 63, 62-96.

Frykman, P. and Deutsch, C. V. (2002) Practical application of geostatistical scaling laws for data integration. *Petrophysics,* 43, 153-171.

García del Cura, M. A., Benavente, D., Martínez-Martínez, J. and Cueto, N. (2012) Sedimentary structures and physical properties of travertine and carbonate tufa building stone. *Construction and Building Materials,* 28, 456-467.

Ghose, R. and Slob, E. C. (2006) Quantitative integration of seismic and GPR reflections to derive unique estimates for water saturation and porosity in subsoil. *Geophysical Research Letters,* 33, L05404.

Gradzinski, M. (2010) Factors controlling growth of modern tufa: results of a field experiment. *In:* Pedley, H. M. & Rogerson, M. (eds.) *Tufas and speleothems: Unravelling the microbial and physical controls.* Geological Society, London, Special Publication 336, 143-191.

Greaves, R. J., Lesmes, D. P., Lee, J. M. and Toksöz, M. N. (1996) Velocity variations and water content estimated from multi-offset, ground-penetrating radar. *Geophysics,* 61, 683-695.

Guo, L. and Riding, R. (1994) Origin and diagenesis of Quaternary travertine shrub fabrics, Rapolano Terme, central Italy. *Sedimentology,* 41, 499-520.

Guo, L. and Riding, R. (1998) Hot-spring travertine facies and sequences, Late Pleistocene, Rapolano terme, Italy. *Sedimentology,* 45, 163-180.

Harbi, H. and McMechan, G. A. (2011) Modeling 3D porosity and permeability from GPR data in the Ellenburger Dolomite, central Texas. *Geophysics,* 76, J35-J46.

Huisman, J., Hubbard, S., Redman, J. and Annan, A. (2003) Measuring soil water content with ground penetrating radar. *Vadose Zone Journal,* 2, 476-491.

Kearey, P., Brooks, M. and Hill, I. (2002) An introduction to geophysical exploration, Blackwell.

Kenter, J. A. M., Braaksma, H., Verwer, K. and van Lanen, X. M. T. (2007) Acoustic behavior of sedimentary rocks: geologic properties versus Poisson's ratios. *The Leading Edge,* April 2007, 436-444.

Knight, R. (2001) Ground penetrating radar for environmental applications. *Annual Reviews of Earth and Planetary Sciences,* 29, 229-255.

Koesoemadinata, A. P. and McMechan, G. A. (2003) Correlations between seismic parameters, EM parameters, and petrophysical/petrological properties for sandstone and carbonate at low water saturations. *Geophysics,* 68, 870-883.

Linares, R., Rosell, J., Roque, C. and Gutiérrez, F. (2010) Origin and evolution of tufa mounds related to artesian karstic springs in Isona area (Pyrenees, NE Spain). *Geodinamica Acta,* 23, 129-150.

Melón, P. and Alonso-Zarza, A. M. (2018) The Villaviciosa tufa: a scale model for an active cool water tufa system, Guadalajara (Spain). *Facies,* 64, 1-16.

Mount, G. J. and Comas, X. (2014) Estimating porosity and solid dielectric permittivity in the Miami Limestone using high-frequency ground penetrating radar (GPR) measurements at the laboratory scale. *Water Resources Research,* 50, 7590-7605.

Mount, G. J., Comas, X. and Cunningham, K. J. (2014) Characterization of the porosity distribution in the upper part of the karst Biscayne aquifer using common offset ground penetrating radar, Everglades National Park, Florida. *Journal of Hydrology,* 515, 223-236.

Nagtegaal, P. J. C., Van Vliet, A. and Brouwer, J. (1983) Syntectonic coastal offlap and concurrent turbidite deposition: The Upper Cretaceous Aren sandstone in the South-Central Pyrenees, Spain. *Sedimentary Geology,* 34, 185-218.

Neal, A. (2004) Ground-penetrating radar and its use in sedimentology: principles, problems and progress. *Earth-Science Reviews,* 66, 261–330.

Neal, A., Grasmueck, M., McNeill, D. F., Viggiano, D. A. and Eberli, G. P. (2008) Full-resolution 3D radar stratigraphy of complex oolitic sedimentary architecture: Miami Limestone, Florida, U.S.A. *Journal of Sedimentary Research,* 78, 638-653.

Pedley, H. M., Hill, I., Denton, P. and Brasington, J. (2000) Three-dimensional modelling of a Holocene tufa system in the Lathkill Valley, north Derbyshire, using ground-penetrating radar. *Sedimentology,* 47, 721-737.

Pellicer, X. M., Corella, J. P., Gutierrez, F., Roques, C., Linares, R., Carbonel, D., Zarroca, M., Guerrero, J. and Comas, X. (2016) Sedimentological and palaeohydrological characterization of Late Pleistocene and Holocene tufa mound palaeolakes using trenching methods in the Spanish Pyrenees. *Sedimentology,* 63, 1786–1819

Pellicer, X. M., Linares, R., Gutiérrez, F., Comas, X., Roqué, C., Carbonel, D., Zarroca, M. and Rodríguez, J. A. P. (2014) Morpho-stratigraphic characterization of a tufa mound complex in the Spanish Pyrenees using ground penetrating radar and trenching, implications for studies in Mars. *Earth and Planetary Science Letters,* 388, 197-210.

Pickett, G. R. (1963) Acoustic character logs and their applications in formation evaluation. *Journal of Petroleum Technology,* 15, 659-667.

Possato, S., Saito, M. A., Curtis, M. P. and Martinez, R. D. (1984) Interpretation of 3-dimensional seismic attributes contributes to stratigraphic analysis of Pampo oil field. *Geophysics,* 49, 653.

Puigdefabregas, C., Muñoz, J. A. and Vergés, J. (1992) Thrusting and foreland basin evolution in the Southern Pyrenees. *In:* McClay, K. (ed.) *Thrust tectonics.* Dordrecht: Springer.

Pujalte, V. and Schmitz, B. (2005) Revisión de la estratigrafía del Grupo Tremp («Garumniense», Cuenca de Tremp-Graus, Pirineos meridionales). *Geogaceta,* 38, 79-82.

Raymer, L. L., Hunter, E. R. and Gardner, J. S. 1980. An improved transit-to-porosity transform (abstract). Society of Professional Well Log Analysts 21st Annual Logging Symposium.

Regnet, J.-B., Fortin, J., Nicolas, A., Pellerin, M. and Guéguen, Y. (2019) Elastic properties of continental carbonates: From controlling factors to an applicable model for acoustic-velocity predictions. *Geophysics,* 84, MR45-MR59.

Reijmer, J. J. G., Blok, C. N., El-Husseiny, A., Kleipool, L. M., Hogendorp, Y. C. K. and Alonso-Zarza, A. M. (2022) Petrophysics and sediment variability in a mixed alluvial to lacustrine carbonate system (Miocene, Madrid Basin, Central Spain). *The depositional record,* 8, 317-339.

Robinson, D. A., Jones, S. B., Wraith, J. M., Or, D. and Friedman, S. P. (2003) A review of advances in dielectric and electrical conductivity measurement in soils using time domain reflectometry. *Vadose Zone Journal,* 2, 444-475.

Ronchi, P. and Cruciani, F. (2015) Continental carbonates as a hydrocarbon reservoir, an analog case study from the travertine of Saturnia, Italy. *AAPG Bulletin,* 99, 711–734.

Rosell, J., Gómez-Gras, D. and Linares, R. 1994. *Mapa Geológico de España a escala 1:50.000, Hoja n◦ 290 (Isona)*. Madrid: Instituto Geológico y Minero de España.

Rosell, J., Linares, R. and Llompart, C. (2001) El "Garumniense" Prepirenaico. *Revista de la Sociedad Geologica de Espana,* 14, 47-56.

Rossi, A. P., Neukum, G., Pondrelli, M., van Gasseldt, S., Zegers, T., Hauber, E., Chicarro, A. and Foing, B. (2008) Large-scale spring deposits on Mars? *Journal of Geophysical Research,* 113, E08016.

Schön, J. (2011) Physical properties of rocks*,* Amsterdam, Elsevier.

Singh, B. (2007) Wave propagation in an orthotropic micropolar elastic solid. *International Journal of Solids and Structures,* 44, 3638-3645.

Soete, J., Kleipool, L. M., Claes, H., Hamaekers, H., Kele, S., Özkul, M., Foubert, A., Reijmer, J. J. G. and Swennen, R. (2015) Acoustic properties in travertines and their relation to porosity and pore types. *Marine and Petroleum Geology,* 59, 320-335.

Storvoll, V. and Bjørlykke, K. (2004) Sonic velocity and grain contact properties in reservoir sandstones. *Petroleum Geoscience,* 10, 215-226.

Topp, G. C., Davis, J. L. and Annan, A. P. (1980) Electromagnetic determination of soil water content: Measurements in coaxial transmission lines. *Water Resources Research,* 16, 574-582.

Vasquez, G. F., Morschbacher, M. J., dos Anjos, C. W. D., Silva, Y. M. P., Madrucci, V. and Justen, J. C. R. (2019) Petroacoustics and composition of presalt rocks from Santos Basin. *The Leading Edge,* May 2019, 342-348.

Vergés, J., Fernàndez, M. and Martínez, A. (2002) The Pyrenean orogen: pre-, syn-, and post-collisional evolution. *Journal of the Virtual Explorer,* 8, 55-74.

Verwer, K., Braaksma, H. and Kenter, J. A. M. (2008) Acoustic properties of carbonates: Effects of rock texture and implications for fluid substitution. *Geophysics,* 73, B51-B65.

Waxman, M. H. and Smits, L. J. M. (1968) Electrical conductivities in oil-bearing shaly sands. *Society of Petroleum Engineers Journal,* 8, 107-122.

Weger, R. J., Eberli, G. P., Baechle, G. T., Massaferro, J. L. and Sun, Y.-F. (2009) Quantification of pore structure and its effect on sonic velocity and permeability in carbonates. *American Association of Petroleum Geologists Bulletin,* 93, 1297-1317.

Wyllie, M. R. J., Gregory, A. R. and Gardner, G. H. F. (1958) An experimental investigation of factors affecting elastic wave velocities in porous media. *Geophysics,* 23, 459-493.

Xu, S. and Payne, M. A. (2009) Modeling elastic properties in carbonate rocks. *The Leading Edge,* January 2009, 66-74.

Yardley, G. S., Graham, G. and Crampin, S. (1991) Viability of shear-wave amplitude versus offset studies in anisotropic media. *Geophysical Journal International,* 107, 493-503.

782 **Table 1:** Petrography.

Lithotype	Fabric	Pore space, cement	Occurs in which facies
Peloidal	massive; microfacies of 35-40% peloids (20-40 µm), 5% silt-sized quartz, 1-2% shell fragments ≤300 µm long; overprinted by 10-30 µm sized microspar crystals, which are difficult to separate from cement	isometric intergranular and intercrystalline matrix pores, mm-scale open fractures and irregular-cylindrical vugs, some with remains of vegetative organic material Dominant pore type: intergranular/intercrystalline 30-40% equigranular sparite cement (20-60 µm)	mainly vent, also older 'La Cassola' slope (sample SL-10)
Thrombolitic	massive-clotted; microfacies of micritic and microsparitic mesoclots (0.5-2 mm) composed of peloidal clots (100-500 µm), clusters of sparry shrubs (0.2-2 mm), and recrystallised ostracod shells (<500 µm)	mm-scale growth framework and shell mouldic pores Dominant pore type: framework/mouldic 20-35% cement, equigranular blocky sparite (20-40 µm) lines larger pores, and drusy sparite (10-50 µm) entirely fills smaller pores	older 'La Cassola' rim
Sparry shrub	mm- to cm-scale crude bedding; microfacies with shrubs (≤1.5 cm high, ≤2 mm wide, (≤2 mm high in cascade sample) of hollow or micrite-filled tubes (15-25 µm diameter) encrusted by blocky sparite (100-600 µm); peloids (20-100 µm) locally within shrubs or creating bedding	growth framework pores, intercrystalline pores, cm-scale elongate mouldic pores after vegetation Dominant pore type: framework/mouldic 5-15% cement (20-25% where shrubs are better developed), interlocking sparite crystals (20-50 µm) cementing framework	cascade, younger 'Basturs' rim and slope (sample SL-02)
Peloidal shrub	massive or crudely cm-bedded; microfacies of 30-40% peloids (40-150 µm) that locally develop into thrombolites and mm-size branching peloidal shrubs, local sparry shrubs (<3 mm high), ostracods	intercrystalline, mm/cm-scale vuggy, framework and mouldic porosity after vegetation Dominant pore type: vug/mould 25-35% cement, equigranular and acicular sparite and microspar (10-60 µm)	slope, transitional between peloidal (older slope samples) and sparry shrub (younger slope samples)
Oncoidal	(clotted) micrite groundmass; oncoids ≤2x4 mm, clotted microsparitic centre surrounded by wavy laminae (20-100 µm thick) and mm-scale botryoids (pseudo-stromatolitic)	intercrystalline and intergranular porosity, vegetation moulds and vugs Dominant pore type: intergranular/intercrystalline 15-25% cement, microspar	pool stromatolites

783

784

Table 2: Digital image analysis parameters.

Thin section image	Gas porosity (plug) (%)	Image analysis porosity (%)	Median pore area (mm^2)	Minimum pore area (mm^2)	Maximum pore area (mm^2)	D50 (mm^2)	DomSize (μm^2)	Median PoA (mm^{-1})	Circularity	Aspect Ratio
CS-01	43.0	22.5	0.00020	0.00003	0.46867	0.00020	180.6	309.7	0.630	2.002
RM-07_1	42.6	15.8	0.00045	0.00010	0.52946	0.00044	154.5	229.5	0.485	2.112
RM-07_2	42.6	15.9	0.00015	0.00003	0.53269	0.00014	154.9	371.2	0.600	2.076
RM-09_1	18.5	6.7	0.00018	0.00003	0.41274	0.00019	223.7	314.6	0.662	2.095
RM-09_2	18.5	5.1	0.00010	0.00003	0.41559	0.00011	138.6	427.8	0.630	2.297
SL-02_1	38.6	15.8	0.00027	0.00006	0.47242	0.00028	137.9	279.2	0.563	2.127
SL-02_2	38.6	13.5	0.00012	0.00003	0.62683	0.00012	120.9	382.5	0.682	2.172
SL-05	34.2	5.1	0.00007	0.00002	0.13981	0.00006	167.6	557.1	0.564	2.171
SL-10	23.8	2.5	0.00008	0.00001	0.02103	0.00007	18.4	463.9	0.741	1.947
ST-11_1	n.d.	4.6	0.00026	0.00003	0.34251	n.d.	156.9	251.3	0.732	2.002
ST-11_2	n.d.	9.3	0.00021	0.00003	2.49961	n.d.	519.9	275.7	0.734	1.922
VT-08_1	22.5	6.0	0.00015	0.00001	0.00499	0.00015	18.5	451.5	0.476	0.529
VT-08_2	22.5	2.0	0.00010	0.00001	0.00164	0.00009	9.1	527.8	0.472	0.513

n.d.: not determined

Table 3: Petrophysical and acoustic data acquired in this study.

Facies	Sample	Plug subsample	He porosity	He permeability (mD)	Vp (m/s)	Vs (m/s)	Vp/Vs	Poisson's ratio	Impedance	Notes
Vent	VT-08	VT-08-N	0.233	97.33	n.d.#	n.d.#				sample also used for electro-magnetic laboratory analyses
	VT-08	VT-08-B	0.225	1.70	6197.44	2810.47	2.21	0.37	n.d.*	
	VT-08	VT-08-C	0.235	2.00	5732.91	2573.30	2.23	0.37	11.58	
Rim	RM-07	RM-07-A	0.361	7600.00	2521.15	1560.71	1.62	0.19	4.24	
	RM-07	RM-07-B	0.426	8200.00	2746.80	1617.07	1.70	0.23	4.14	
	RM-09	RM-09-N	0.191	188.60	n.d.#	n.d.#				sample also used for electromagnetic laboratory analyses
	RM-09	RM-09-A	0.185	32.00	5670.36	2858.61	1.98	0.33	12.38	
Slope	SL-02	SL-02-HN	0.398	619.70	n.d.#	n.d.#				sample also used for electro-magnetic laboratory analyses
	SL-02	SL-02-VN	0.388	1119.85	n.d.#	n.d.#				sample also used for electro-magnetic laboratory analyses
	SL-02	SL-02-V	0.339	6500.00	4489.17	2325.99	1.93	0.32	7.79	
	SL-02	SL-02-H	0.386	8000.00	3047.35	2052.30	1.48	0.08	4.94	
	SL-05	SL-05-V	0.306	1700.00	4724.32	2731.25	1.73	0.25	8.73	
	SL-05	SL-05-H	0.342	2300.00	3852.25	2134.21	1.81	0.28	6.74	
	SL-10	SL-10-N1	0.186	219.11	n.d.#	n.d.#				sample also used for electro-magnetic laboratory analyses
	SL-10	SL-10-N2	0.226	1233.80	n.d.#	n.d.#				sample also used for electro-magnetic laboratory analyses
	SL-10	SL-10-B	0.235	170.00	4601.63	2388.19	1.93	0.32	9.29	
	SL-10	SL-10-C	0.238	N/A	4710.56	2287.21	2.06	0.35	n.d.*	
Cascade	CS-01	CS-01-B	0.430	14000.00	2055.58	901.36	2.28	0.38	2.33	
Pool Stromatolite	ST-11	ST-11	n.d.	n.d.	n.d.	n.d.				sample also used for electro-magnetic laboratory analyses

n.d.: no laboratory analysis carried out
n.d.*: no bulk density calculated
n.d.#: analysis carried out, but results considered unreliable
N/A: analysis failed

Table 4: Electromagnetic data acquired in this study.

Facies	Sample	V (field) (m/ns)	V (dry) (m/ns)	V (wet) (m/ns)	e_{rs}	porosity
Vent	VT-08	0.110	0.119	0.098	4.3	0.144
Rim	RM-07	0.092	n.d.	n.d.	n.d.	n.d.
Rim	RM-09	0.092	0.111	0.092	4.9	0.153
Slope	SL-02	0.092	0.128	0.075	4.2	0.281
Slope	SL-05	0.092	0.160	N/A	4.5	0.215
Slope	SL-10	0.110	0.101	0.099	5.7	0.102
Cascade	CS-01	0.092	0.185	N/A	4.5	0.447
Pool Stromatolite	ST-11	0.110	0.151	0.059	3.4	0.456

n.d.: no laboratory analysis carried out (no dedicated sample)
N/A: analysis failed

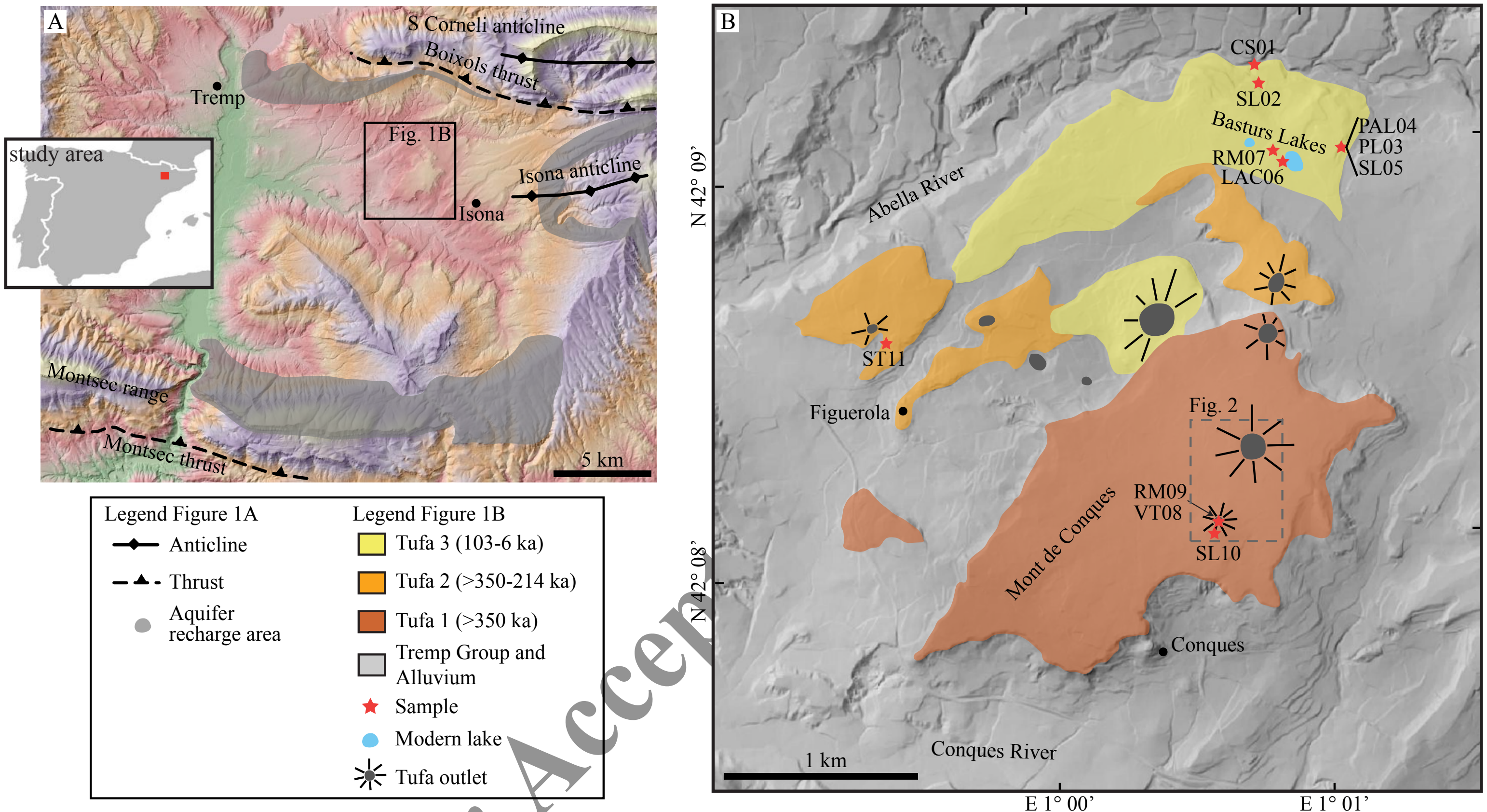

Figure 1: (A) Location of the Tremp Basin and main groundwater recharge areas. (B) Geomorphological map of the ITMC with sample locations. Location of Figure 2 (La Cassola and El Colector outlets) is indicated by grey box. Modified from Pellicer et al. (2014).

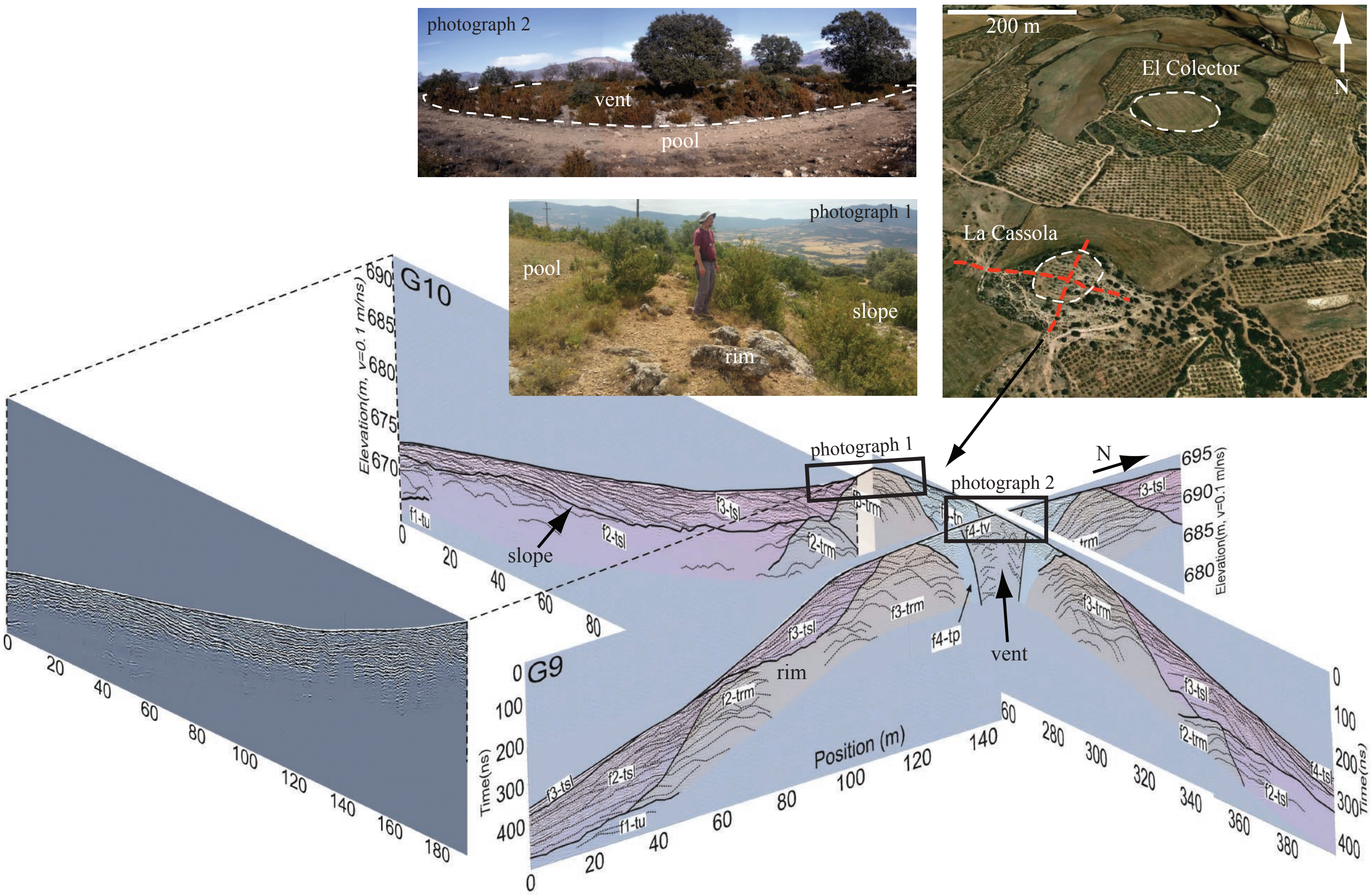

Figure 2: Fence diagram showing the interpreted GPR profiles and mound architecture in La Cassola (for location see top right inset and Figure 1B). Photographs 1 and 2 illustrate typical outcrop morphologies. Modified from Pellicer et al. (2014).

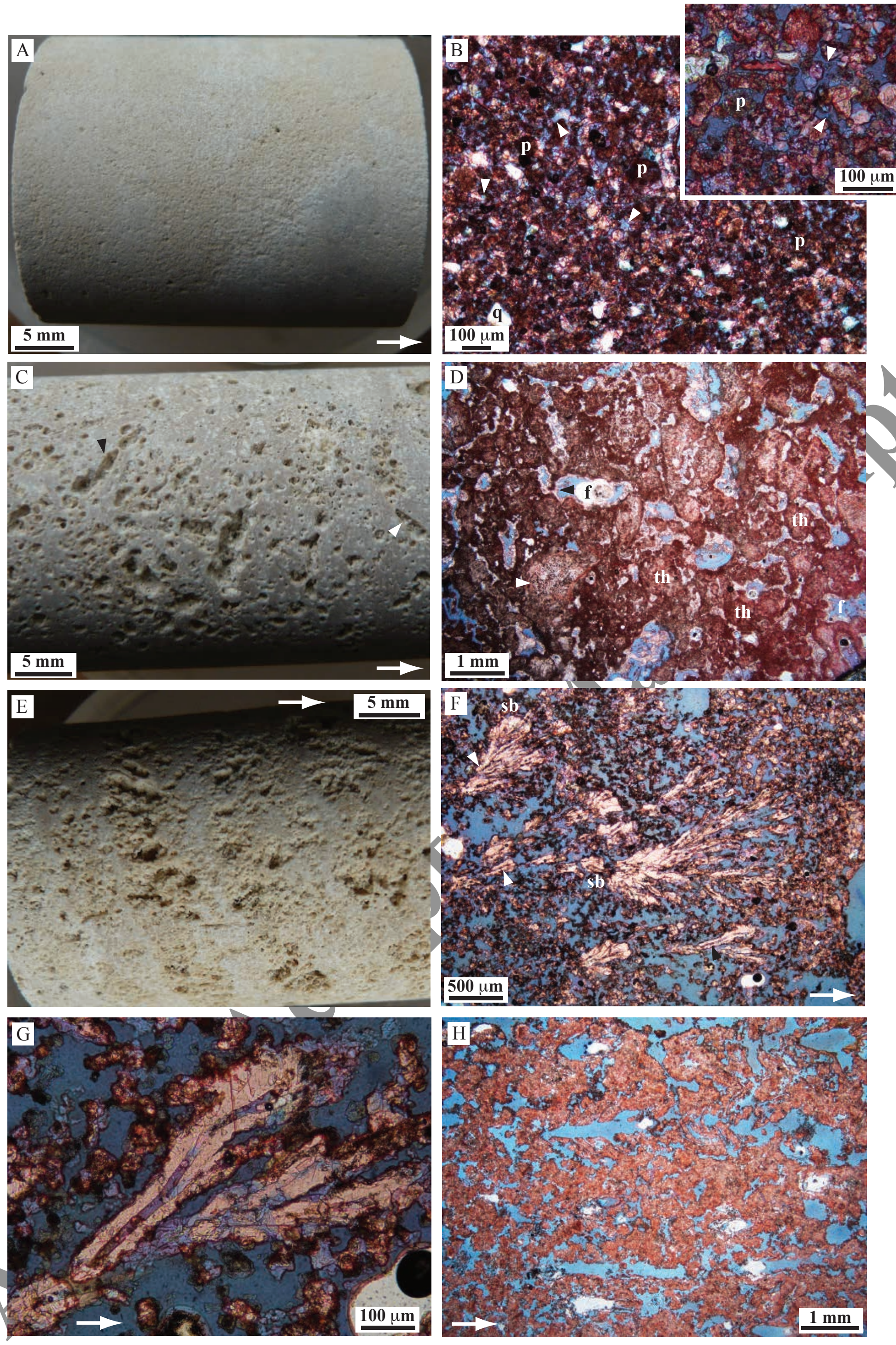

Figure 3: (A and B) Peloidal lithotype: (A) Plug (sample VT-08). (B) Microfacies of peloids (p) and minor quartz (q), with isometric interparticle and intercrystalline pores (white arrows) (sample VT-08). The inset is an enlargement of this lithotype to illustrate the microsparitic crystalline nature of the fabric. (C and D) Thrombolitic lithotype: (C) Plug with µm-scale to mm-scale framework pores and moulds (black arrow), some after gastropods (white arrow) (sample RM-09). (D) Microfacies of clotted peloidal thrombolite (th) with local sparry shrubs

(white arrow). Porosity is framework (f) and mouldic. Pores are lined by sparite cement (black arrow) (sample RM-09). (E through H) Sparry shrub lithotype: (E) Plug with crude bedding (sample SL-02). (F) Microfacies of branching sparry shrubs (sb), some preserving central tubes (white arrows). The shrub indicated by a black arrow is enlarged in (G). The porosity is framework, intercrystalline and mouldic after vegetation (sample CS-01). (G) Detail of shrub highlighted by black arrow in (F), showing the sparite-coated tubes. (H) Recrystallised sparry shrub lithotype with upright large pores. Shapes suggest moulds after vegetation, possibly bryophytes (sample RM-07). Large white arrows indicate ‘up’.

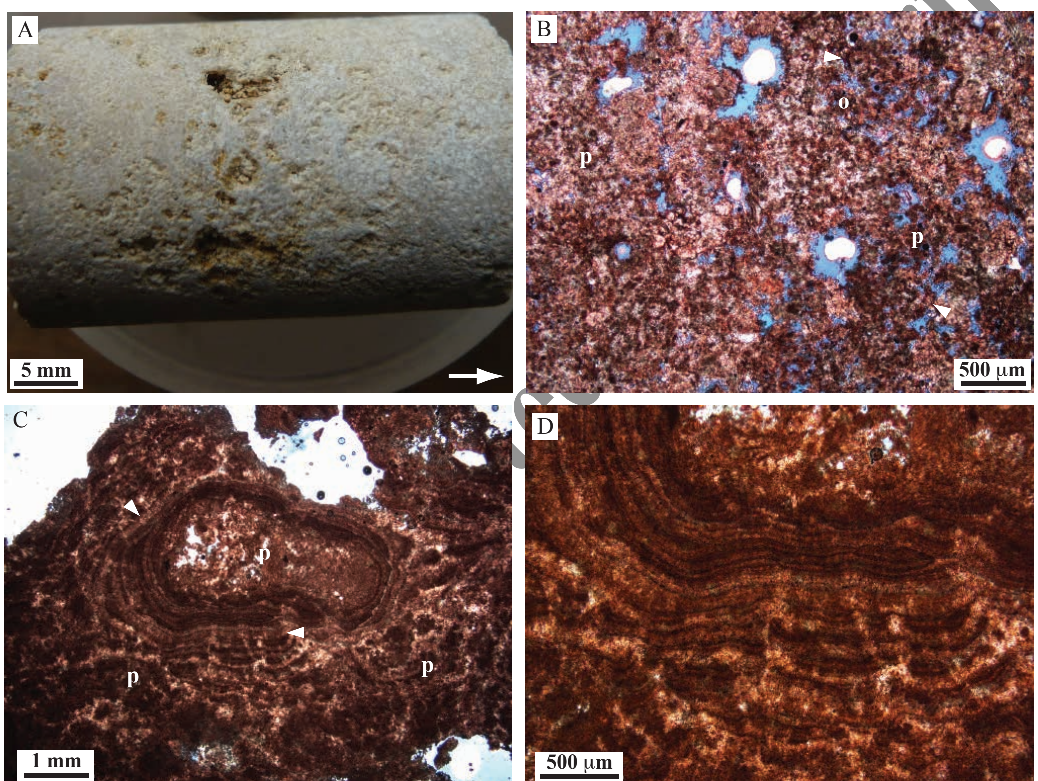

Figure 4: (A and B) Peloidal shrub lithotype: (A) Plug (sample SL-10). (B) Microfacies of clumped peloidal fabric (p), with peloids locally arranged into branching shrubs (white arrows). Rare ostracods are present (o). Intercrystalline, framework and vuggy pores (sample SL-05). (C and D) Oncoidal lithotype: (C) Oncoid (white arrows) around microsparitic centre with clumped peloidal groundmass (p). Pores are interparticle, intercrystalline and vuggy (sample ST-11). (D) Detail of (C) illustrating the fine micritic lamination and botryoids in oncoid. Large white arrows indicate ‘up’.

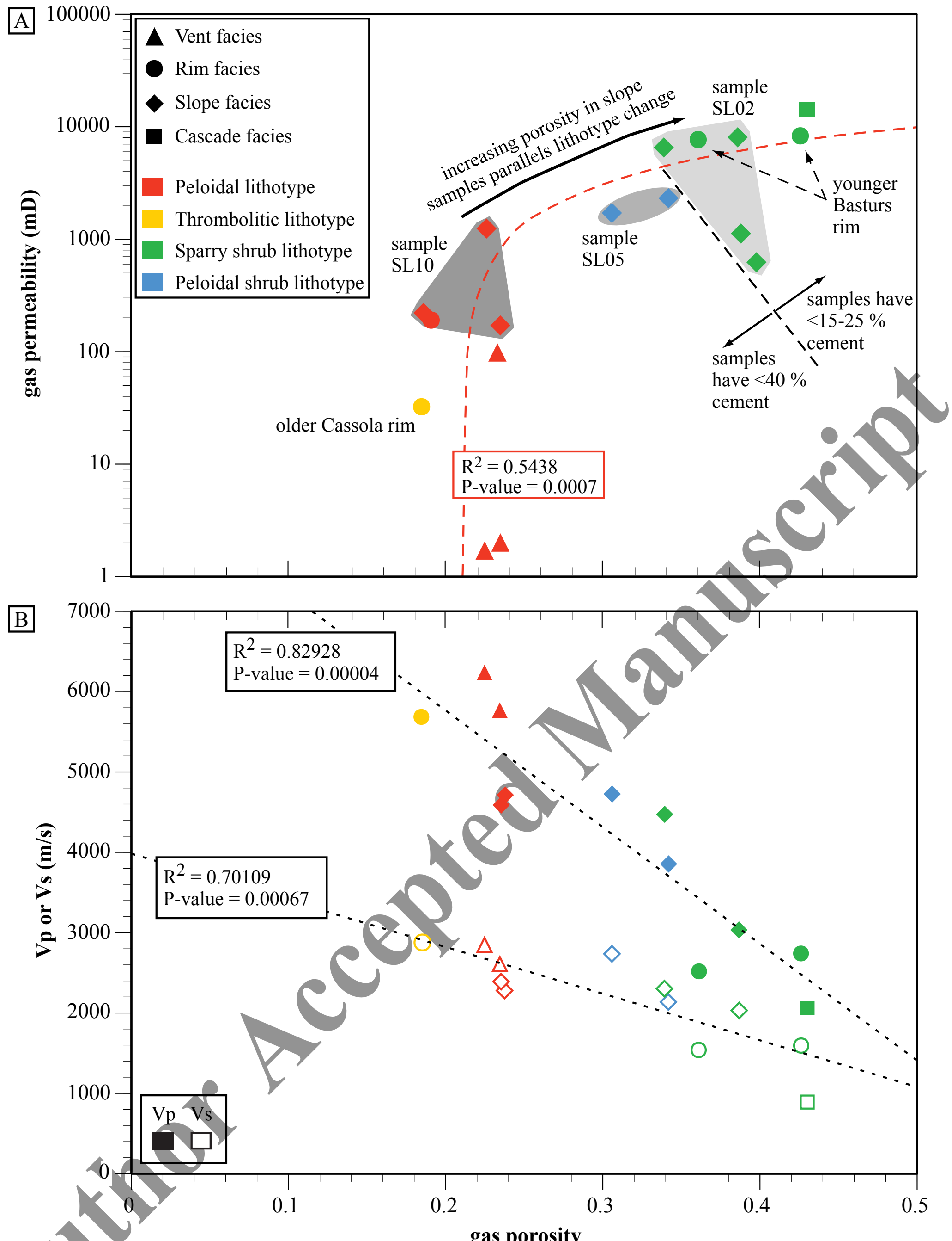

Figure 5: (A) Gas porosity versus permeability for the ITMC data set, plotted according to facies (symbols) and lithotypes (colours). Note that no porosity-permeability pair was obtained for pool facies/oncoidal lithotype. Slope samples are highlighted that show a progressive increase in porosity, which is related to changes in lithotype from more peloidal to sparry shrub. (B) Gas porosity versus Vp and Vs. Data are plotted according to facies (symbols) and lithotype (colours).

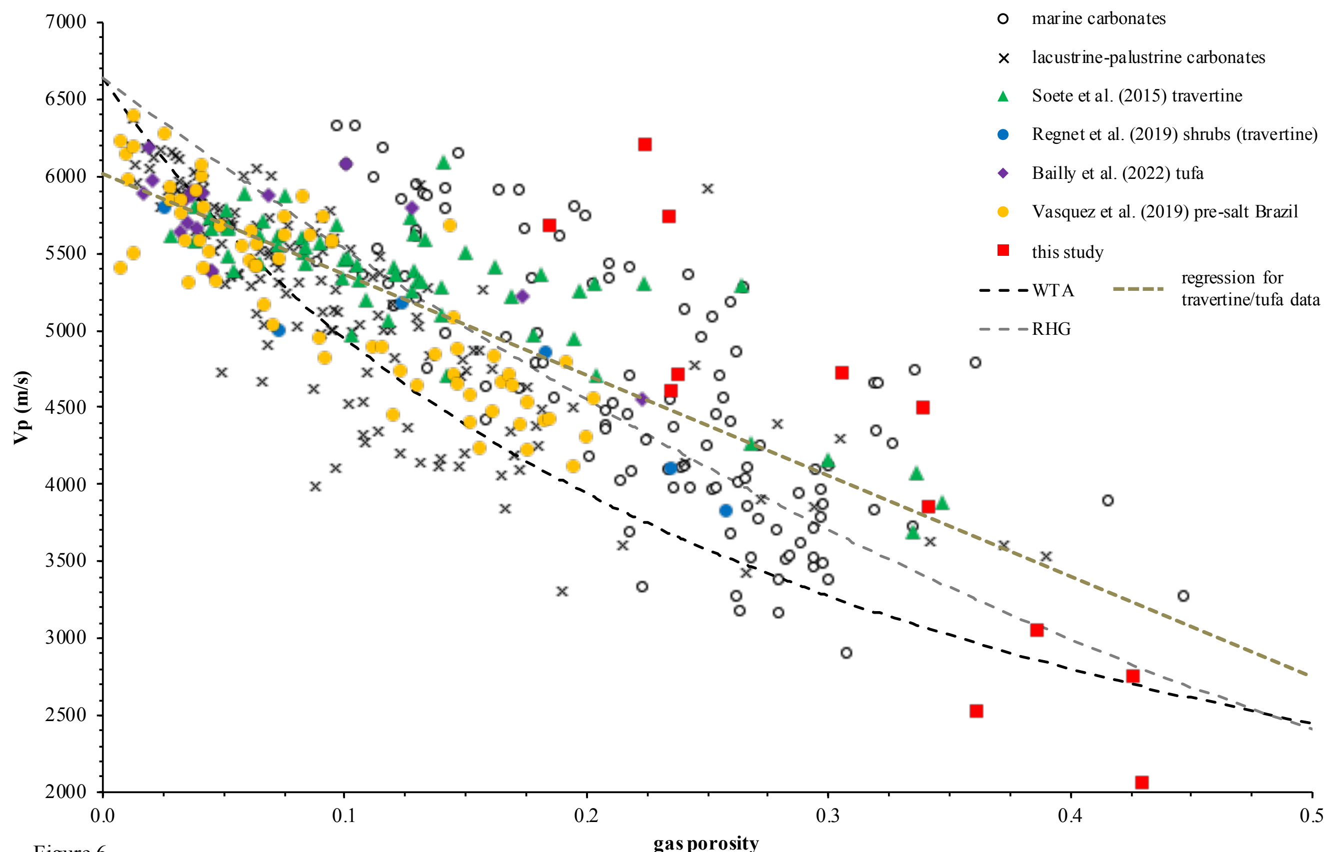

Figure 6

Figure 6: Gas porosity versus Vp for the current data set compared against various published data sets of marine (Eberli et al., 2012; Weger et al., 2009) and continental carbonates. The group of lacustrine-palustrine carbonates includes allochthonous carbonates from Regnet et al. (2019) (samples ≥ 95% carbonate, coquinas and bioclastic wacke/packstone), Reijmer et al. (2022) (samples ≥ 95% carbonate), and Bailly et al. (2022) (facies F5, F6, F8, F9). Shrub data from Regnet et al. (2019) include samples with < 95% carbonate, whereas data from Vasquez et al. (2019) are restricted to samples ≥ 98% carbonate. Tufa from Bailly et al. (2022) only include phytoherm framestones (facies F7). Time average lines are plotted for comparison (WTA: Wyllie Time Average; RHG: Raymer-Hunt-Gardner).

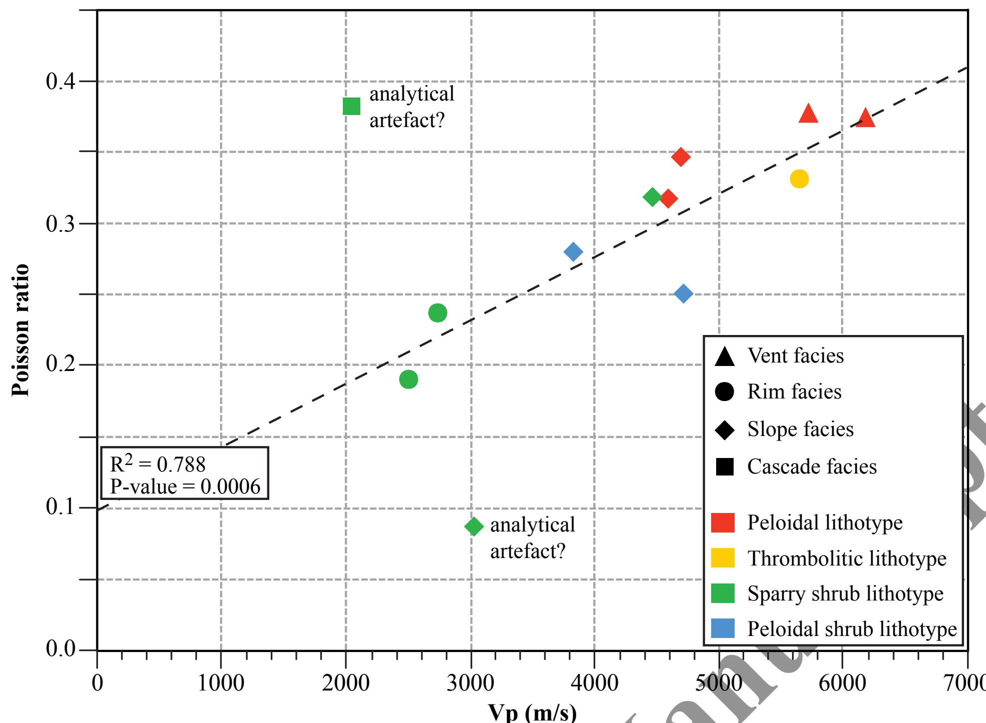

Figure 7: Poisson's ratio plotted as a function of Vp. Data are plotted according to facies (symbols) and lithotype (colours). Two outlier samples are indicated, which could be analytical artefacts of acoustic measurements, or realistic data. The linear regression shown does not take these samples into account.

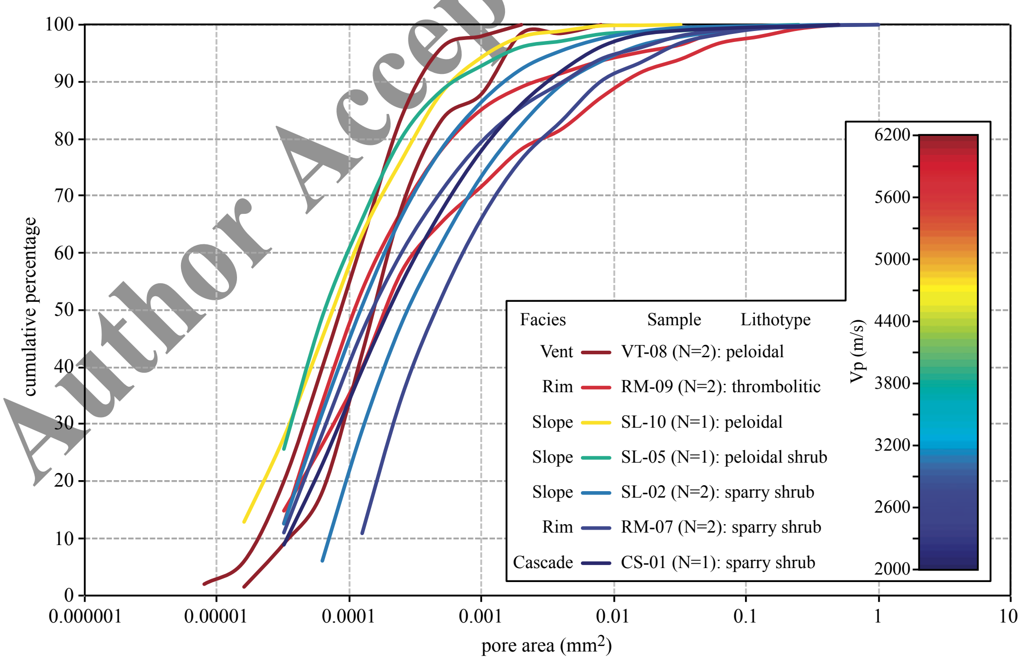

Figure 8: Cumulative pore area curves derived from image analysis. Colours represent Vp measured on corresponding plugs. The lithotype determined on thin sections is given as well. Image analysis on the two pool stromatolite samples was considered unreliable, and these samples are excluded from the graph.

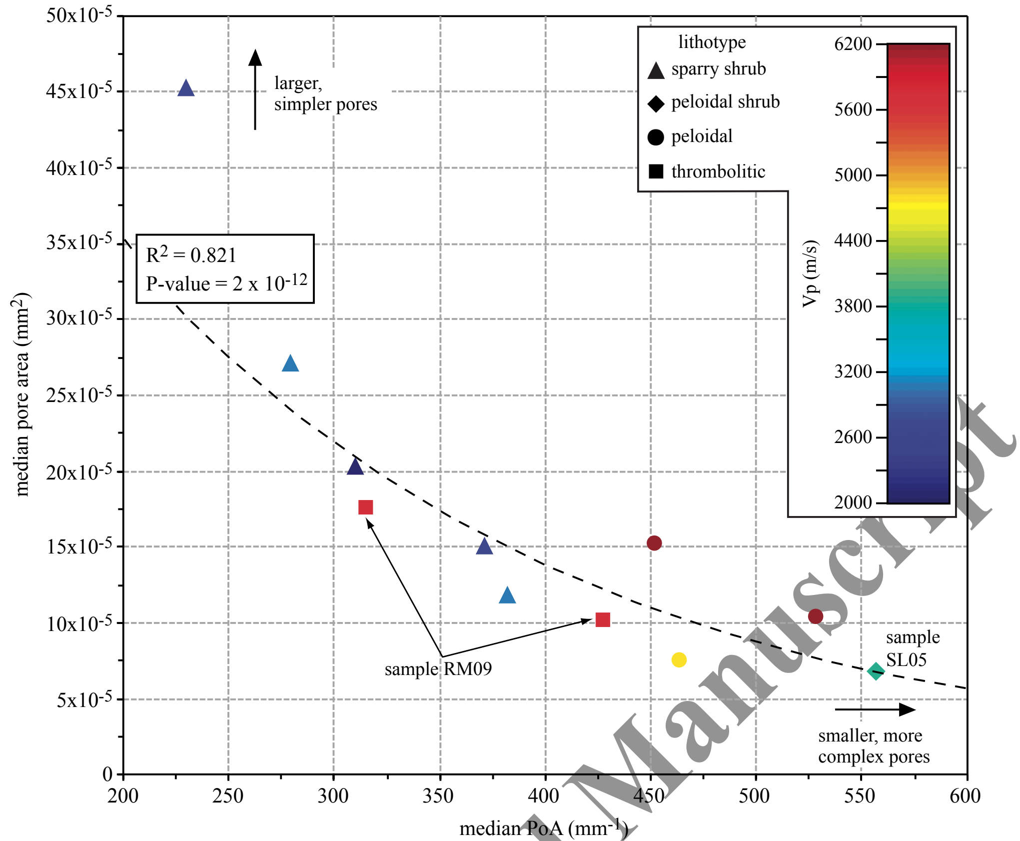

Figure 9: Perimeter over Area (median PoA) against median pore area. Colours represent Vp, whereas the symbols reflect the observed lithotypes. Two pool stromatolite samples are excluded from the graph.

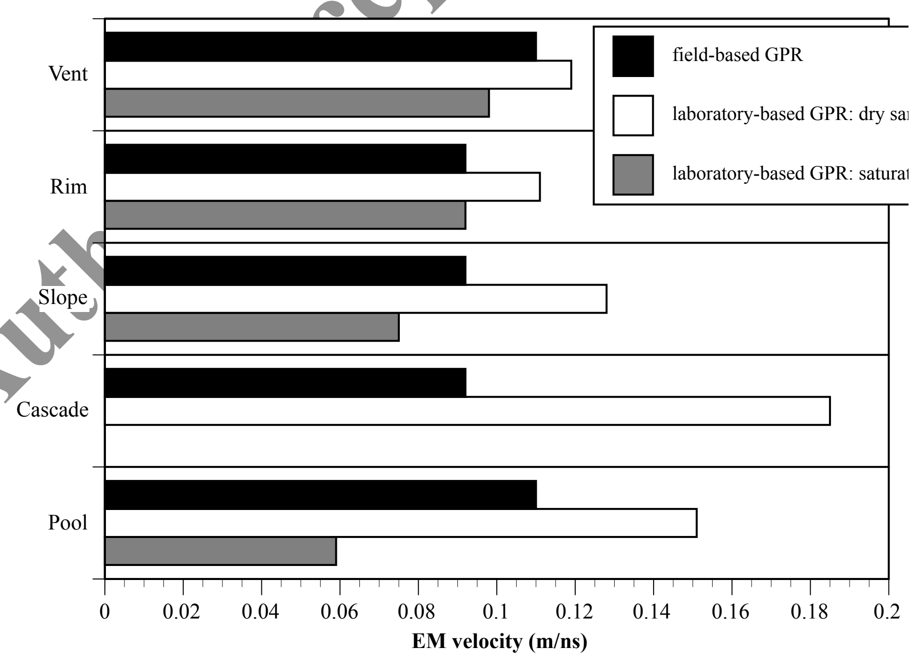

Figure 10: Comparison of electromagnetic wave velocities for different morphological elements, estimated in the laboratory under completely dry and saturated conditions (this study), and estimates from field-based GPR from Pellicer et al. (2014).

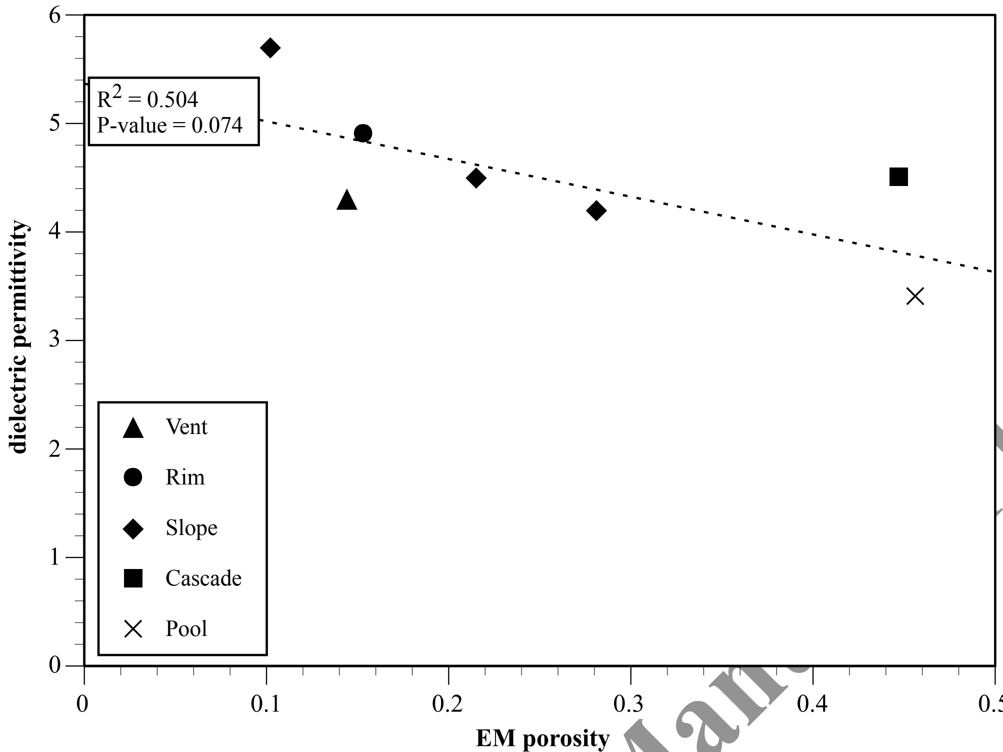

Figure 11: Linear dependence of solid dielectric permittivity on CRIM model porosity. Data are plotted according to facies.

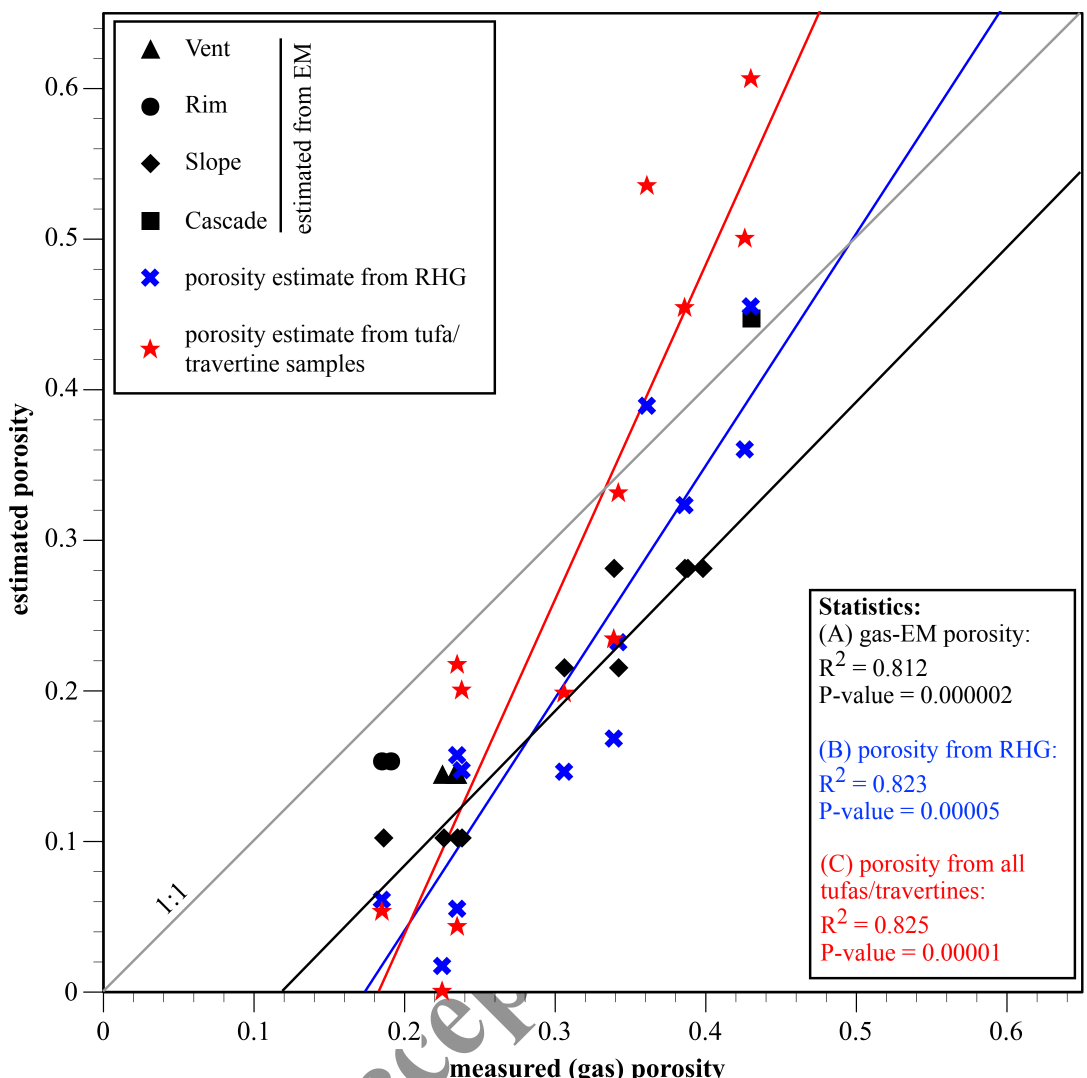

Figure 12: Comparison of measured gas porosity against porosity derived from the methods applied in this study: (A, black data points) EM porosity calculated from the CRIM model (equation 10), (B, blue data points) porosity from Vp (Raymer-Hunt-Gardner equation 6), (C, red data points) porosity from Vp (linear regression of tufa and travertine data in Figure 6, equation 9).

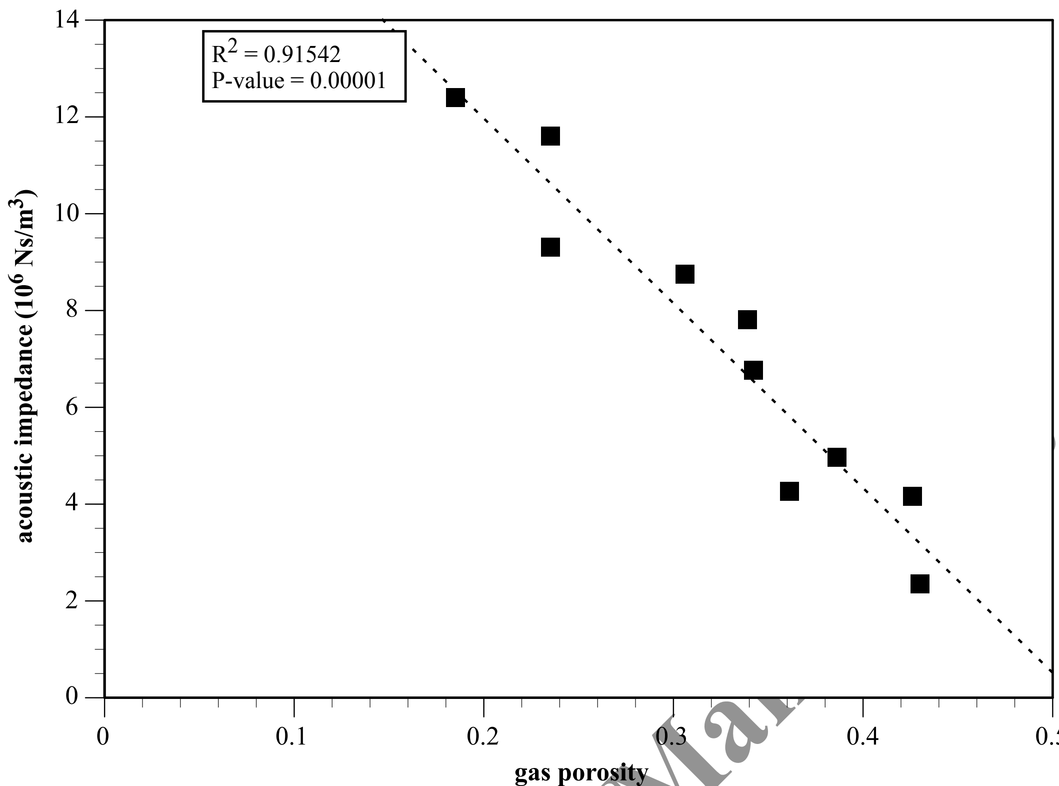

Figure Supplementary Material 1: Gas porosity versus acoustic impedance.

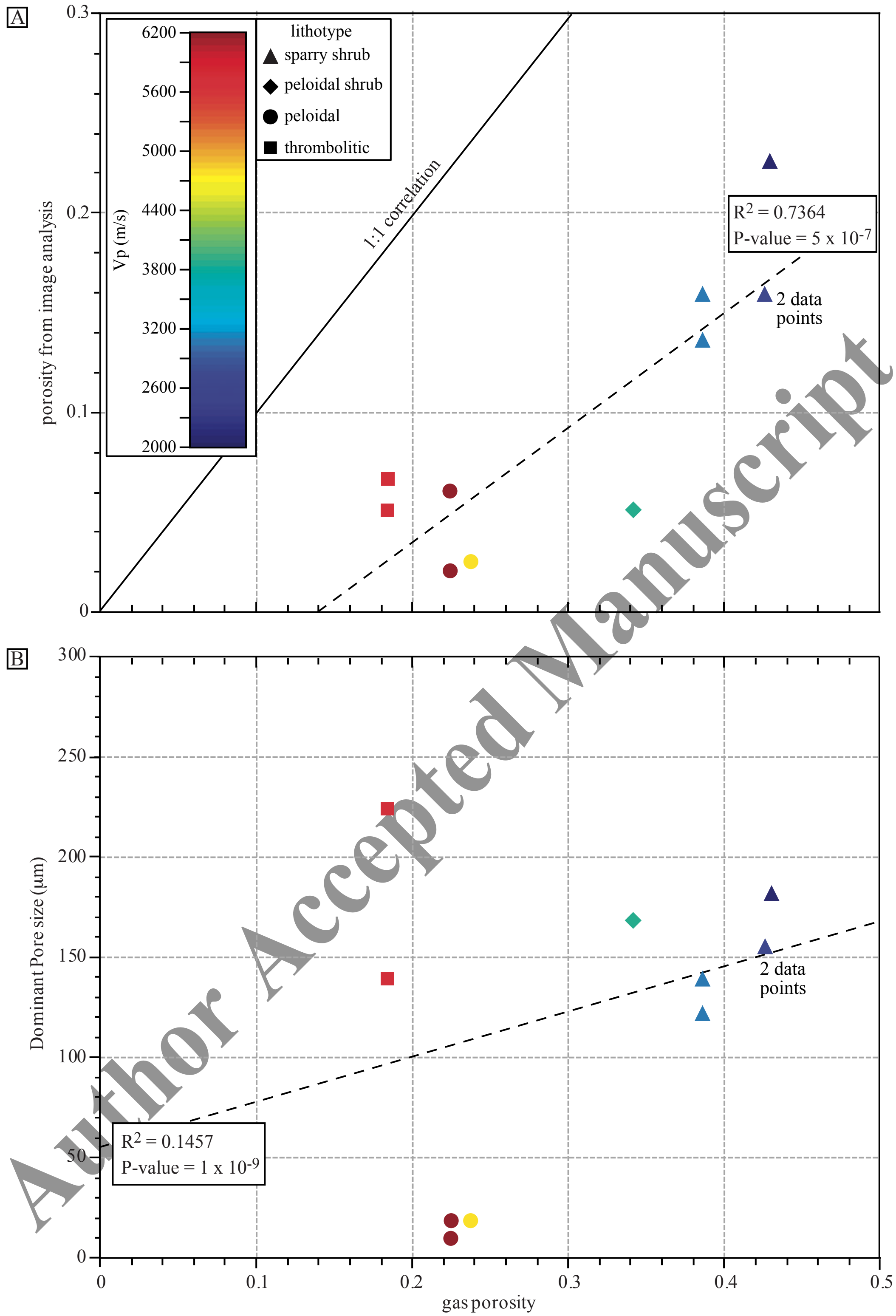

Figure Supplementary Material 2: (A) Measured gas porosity against porosity determined from image analysis. (B) Measured gas porosity against dominant pore size (DomSize) determined from image analysis. Colours in both graphs represent Vp measured on corresponding plugs, whereas the symbols reflect the observed lithotypes.

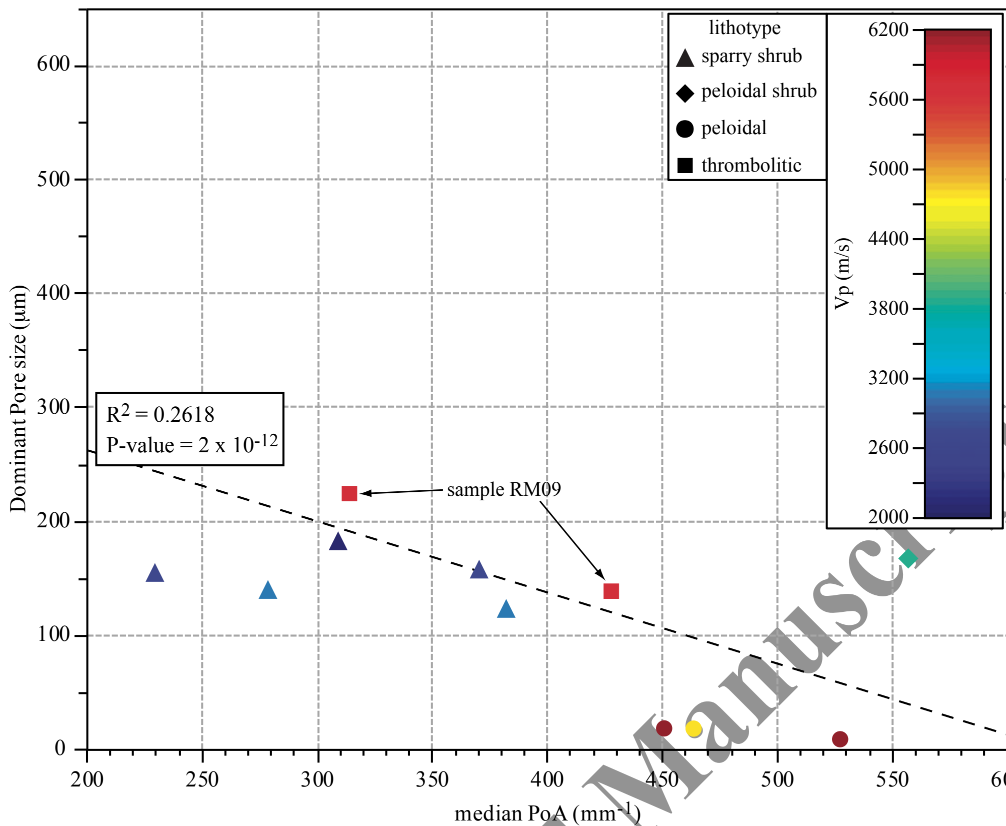

Figure Supplementary Material 3: Median Perimeter over Area (PoA) against dominant pore size (DomSize) determined from image analysis. Colours represent Vp measured on corresponding plugs, whereas the symbols reflect the observed lithotypes.

Acknowledgements

An international mobility grant Jose Castillejo to J.P.C. (CAS19/00311) by the Spanish Ministry of Education, Culture and Sports (MECD) is gratefully acknowledged. The authors wish to thank Matthew McClellan and Katie Bonkowski (Davie) for GPR measurement laboratory support, and Steve May, Lee Paul, and Ernie Rutter (Manchester) for acoustic petrophysical measurement support. Constructive comments by Cathy Hollis, Giovanna Della Porta, and Michał Gradziński on an earlier version, as well as by two anonymous journal reviewers have greatly improved the quality of the manuscript.

Funding sources

This study was partially funded by means of an international mobility grant Jose Castillejo to J.P.C. (CAS19/00311) financed by the Spanish Ministry of Education, Culture and Sports (MECD). The other authors did not receive any specific grant from funding agencies in the public, commercial, or not-for-profit sectors.

Data availability statement: The data that support the findings of this study are available from the corresponding author upon reasonable request.